The Design of a Calorimeter to Measure Concentrated Solar Flux

A Thesis
SUBMITTED TO THE FACULTY OF
UNIVERSITY OF MINNESOTA
BY

Elizabeth Anne Bennett Sefkow

IN PARTIAL FULFILLMENT OF THE REQUIREMENTS
FOR THE DEGREE OF
MASTER OF SCIENCE

Dr. Jane H. Davidson, Adviser

April 2013

Acknowledgements

I would like to thank the following people for their contributions to this work:

- My adviser, Dr. Jane H. Davidson, for her guidance and support throughout my research experience
- Dr. Jörg Petrasch for the use of VeGas
- All of my colleagues in the solar lab between 2011 and 2013 who have given me feedback and assistance

I would also like to thank my family and friends for all of their love, support, and encouragement.

Abstract

A water-cooled, cavity calorimeter was designed to accurately measure concentrated solar thermal power produced by the University of Minnesota's solar simulator. The cavity is comprised of copper tubing bent into spiral and helical coils for the base and cylindrical walls, respectively. Insulation surrounds the cavity to reduce heat transfer to the ambient, and a water-cooled aperture cover is positioned at the open end of the cavity. The calorimeter measures the heat gain of water flowing through the system as radiant energy is passed through the aperture. Chilled water flows through the tubing, and the energy incident on the cavity surface is conducted through the wall and convected to the flowing water. The energy increase in the water can be observed by an increase in fluid temperature. A Monte Carlo ray tracing method is used to predict the incident flux distribution and corresponding power on the surfaces of the cavity. These values are used to estimate the thermal losses of the system, and it is found that they account for less that 1% of the total power passed through the aperture. The overall uncertainty of the calorimeter is found by summing the measured uncertainty and the estimated heat loss and is found to be ±2.5% for 9.2 kW of power output and ±3.4% for 3 kW.

Table of Contents

List of Tables

List of Figures

Nomenclature

Latin

A	area, m^2
a	half length of the major axis of an ellipsoidal reflector, m
b	half length of the minor axis of an ellipsoidal reflector, m
C	center point of a circular disk
c	half focal length of a single ellipsoidal reflector, m
c_p	specific heat of water, J kg^{-1} K^{-1}
D	diameter, m
d	diameter, m
F	foot point of geometry (reference point)
f	Darcy-Weisbach friction factor
g	gravitational acceleration, m s^{-2}
h	heat transfer coefficient, W m^{-2} K^{-1}
h_L	head loss, m
HHV	higher heating value, J mol^{-1}
k	thermal conductivity, W m^{-1} K^{-1}
L	length, m
L/R	depth-to-cavity radius ratio
$\dot{m}$	mass flow rate, kg s^{-1}
N	number of turns in helix
N_{ray}	number of rays
Nu	Nusselt number
P_{helix}	pitch of helix, m
P	power, W
p	pressure, Pa
Pr	Prandtl number
q	power, W
q”	flux, W m^2
R	reading
R_{cond}	resistance due to conduction, K W^{-1}
R_{conv}	resistance due to convection, K W^{-1}

r	radius, m
Ra	Rayleigh number
Re	Reynolds number
S	relative strength of lamp
T	temperature, °C
t	thickness, m
u	uncertainty, W
UA	overall heat transfer coefficient-area product, W K^{-1}
v	velocity, m s^{-1}
$\dot{W}$	work, W
x	primary Cartesian position or coordinate, m
y	primary Cartesian position or coordinate, m
z	height, m

Greek

Δ	change in respective quantity
ε_a	apparent emissivity
ε	tube roughness, m
η	efficiency
θ	acceptance angle of solar simulator, °
ν	kinematic viscosity, m^2 s^{-1}
ρ	reflectivity of surface
ρ_f	density of fluid, kg m^{-3}
σ	Stefan-Boltzmann constant, W m^{-2} K^{-4}

Subscripts

15.5kW	pertaining to 15.5kW power input
3kW	pertaining to 3kW power input
air	pertaining to air
avg	average
amb	pertaining to ambient conditions
ap	pertaining to aperture cover
backwall	pertaining to calorimeter back wall
bw	pertaining to cavity base wall

bolt	pertaining to bolt
b	bulk
c	pertaining to cooling coil on aperture cover
ch	characteristic length of cavity
cav	pertaining to cavity
cl	centerline of helix
cond	conduction
conv	convection
cov	pertaining to aperture cover
critical	pertaining to critical Reynolds number for fiction factor correlation
Cu	pertaining to copper
curve	pertains to curve of aperture cooling coil
cut	pertaining to manufacturing parameter
design	pertaining to design parameter
edge	aperture edge
electrical	electric power input to lamp
expansion	tube expansion
fluid	pertaining to respective fluid
fuel	pertaining to fuel
h	pertaining to helix
hole	pertaining to respective hole
hot	pertaining to hot surface
i	inner
in	power output of solar simulator
inc	radiation incident on respective surface
ins	pertaining to insulation
inlet	pertaining to tubing inlet
losses	sum of thermal losses
lost	radiation lost to space
m	mean
measured	pertaining to measured parameter
o	outer
out	power output from simulator

outlet	pertaining to tubing outlet
pump	pertaining to the pump
ref	reflected radiation
rerad	reradiation
s	surface area
solar	pertaining to solar power
solar-to-fuel	pertaining to solar-to-fuel conversion
sol	pertaining to solder
spiral	pertaining to spiral
ss	pertaining to stainless steel
straight	pertaining to a straight tube
thermal	pertaining to thermal power
tube	pertaining to respective tubing
w	wall

Chapter 1

Introduction

1.1 Motivation

When evaluating the performance of a solar thermochemical reactor, an important metric is the efficiency of converting concentrated solar radiation to a chemical fuel. This efficiency is defined as the energy stored in the fuel divided by the energy used to produce the fuel, as shown in equation (1.1). The fuel production rate is given my $\dot{m}_{\text{fuel}}$, the higher heating value of the fuel is HHV_{fuel}, and the input solar thermal power is q_{solar}.

$$\eta_{\text{solar-to-fuel}} = \frac{\dot{m}_{\text{fuel}} \text{HHV}_{\text{fuel}}}{\text{q}_{\text{solar}}} \tag{1.1}$$

To establish a meaningful efficiency, the ability to accurately measure the solar thermal power at the aperture of the reactor is required. At the University of Minnesota, this power source is a high-flux solar simulator that can supply up to 9.2 kW of power to a 6 cm diameter area in its focal plane. It is comprised of seven radiation units each with a high power xenon arc lamp and reflector, and the xenon arc lamps have spectral characteristics close to sunlight.

The current approach used to measure the flux of the simulator is an optical flux measurement method. A water-cooled Lambertian target is placed in the simulator focal plane. The diffuse radiation reflected from the target is viewed by a charge coupled device (CCD) camera through absorptive-reflective neutral density filters and a lens [1]. Direct measurements of the incident radiative flux are taken using a circular foil heat gage, and the grayscale photographs from the camera are then calibrated to the flux measurements to provide a spatial distribution of the flux at the target. The heat flux gage is calibrated by the manufacturer, using a flat black plate and sunlight. Because of the spatial and spectral distribution differences of the radiation produced by the solar simulator to that of sunlight, the gage is recalibrated in-house. An uncertainty of ±12% is associated with the calibration of the heat flux gage [2], and the total uncertainty in the flux measurement is ±12%. A calorimeter is recommended to measure the solar simulator radiative output more accurately.

A calorimeter to measure solar flux primarily consists of a water-cooled cavity or flat-plate. The energy that is absorbed by the water can be directly related to the incident radiative flux and power. Many solar energy research laboratories around the world use calorimeters to measure concentrated thermal power. Pérez-Rábago *et al.* [3] designed and built a cold-water, conical cavity calorimeter to measure the thermal power of a 1.3 kW point focus solar

concentrator system in Mexico. The reported experimental uncertainty is approximately ±4% of the measured flux. The calorimeter consists of two concentric cones and insulation surrounding them. The inner cone is made of copper for high thermal conductivity, while the outer cone is made of stainless steel. Chilled water flows between the cones to absorb the radiative energy from the concentrator (see Fig 1.1). The mass flow rate and inlet and outlet temperatures of the fluid are measured to calculate the amount of energy being absorbed by the water. The geometry of the system is optimized to maximize the apparent absorptivity of the cavity. A numerical heat transfer study was completed using the software package FLUENT. It accounts for radiative energy absorbed by the cavity wall, forced convection of the cooling fluid, conduction through the walls of the system, as well as natural convection between the outer wall and ambient. The simulation prediction and measured results are within 6% of each other, validating the model.

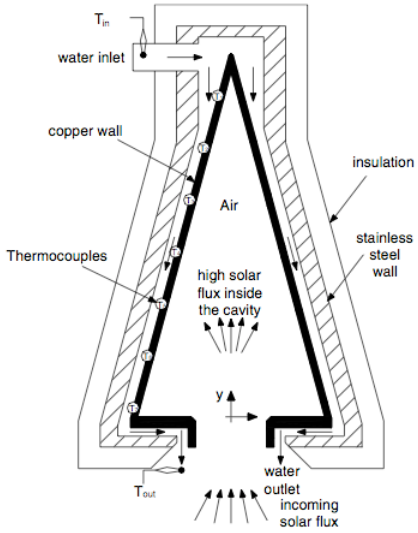

Figure 1.1 Conical cavity calorimeter schematic [3]

Glaser [4] developed a spherical cavity calorimeter. The primary components of the design are a conical aperture, spherical copper receiver, and a cylindrical radiation-shielding jacket. Cooling water absorbs the energy entering the cavity by first flowing around the shielding jacket and then around the receiver; the energy absorbed by the water is then measured. Water flowing over the jacket reduces radiation heat transfer between the receiver and ambient. Glass beads and a zirconia rod hold the receiver in place inside the housing and help minimize conduction between the receiver and housing. The aperture cover is cooled separately so that the only energy measured is what passes through the aperture (see Fig 1.2). Experiments have shown that the receiver can withstand fluxes up to 16,668 kWm^{-2} for extended periods of time and has an uncertainty of ±5% of the measured power.

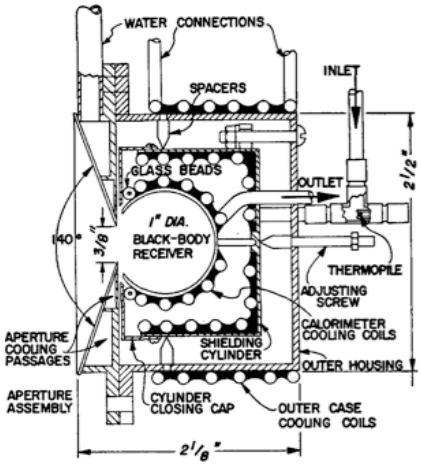

Figure 1.2 Spherical cavity calorimeter schematic [4]

A cylindrical cavity calorimeter by Willoughby [5] is capable of accurately measuring concentrated radiant energy using a null method, which compares radiant energy to electrical energy. Two identical black body receivers both have chilled water flowing through coils embedded in the cylindrical, copper walls that make up the cavities. Both cavities are also equipped with a coil that can pass current through the walls (see Fig 1.3). One of the receivers is exposed to radiative energy, while the other is heated electrically. A differential thermopile measures the difference in temperature between the water outlets of each receiver, and the electrically heated receiver is heated until there is no temperature difference between the two outflows. The amount of radiant energy can be deduced from the amount of electrical energy input into the system. It is stated that this technique has an uncertainty of ±2% of the measured power.

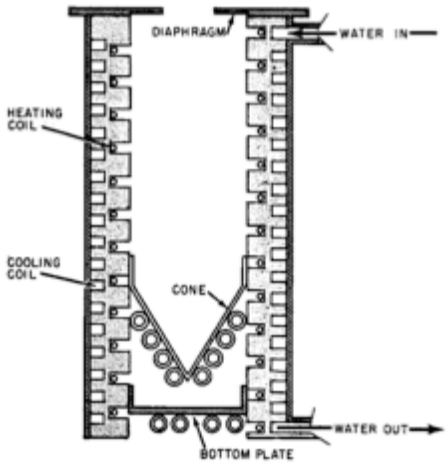

Figure 1.3 Cylindrical cavity calorimeter schematic [5]

A high flux, water flow calorimeter has been developed and tested at DLR Cologne that can measure up to 1 kW of power [6]. The cavity of the calorimeter is a conical shape made from copper, with cooling channels within the wall of the cavity. Insulation surrounds the cavity to minimize heat transfer between the calorimeter and ambient. The aperture cover is water cooled by a separate cooling system. The thermal losses considered in the design are reflection and emission through the aperture, convection through the aperture, conduction through the insulation, and thermal effects from the cooled aperture cover (see Fig 1.4). It has been determined that all of the thermal losses are minor and account for 0.7% of the total power passing through the aperture. A measurement uncertainty of ±0.5% of the power input is associated with the calorimeter.

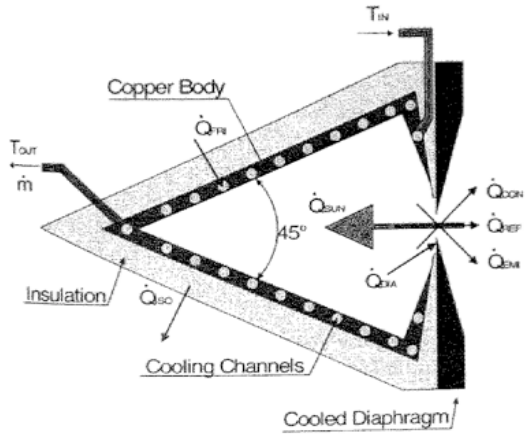

Figure 1.4 DLR Cologne calorimeter [6]

Jaramillo *et al.* [8] designed and built a flat-plate calorimeter to measure the solar flux located at the focus of a 1.3 kW solar concentrator. As shown in Figure 1.5, a flat-plate calorimeter consists of two concentric cylindrical stainless steel tubes, a flow diffuser, a circular copper receiving plate, and insulation. The calorimeter measures the energy incident on the outer surface of the receiving plate by measuring the heat gain of the fluid flowing across the inner surface of the plate. Radiative and convective losses are neglected with the cold-water calorimetry technique. This technique assumes the receiving plate remains at ambient temperature, which is achieved by using highly conductive material and controlling the mass flow rate of the fluid to enhance convective heat transfer. When the heat transfer rate is high enough, the plate temperature will remain close to ambient and thermal losses can be neglected. In this case, the radiation incident on the receiving plate is equal to the amount of heat gain of the fluid in the system.

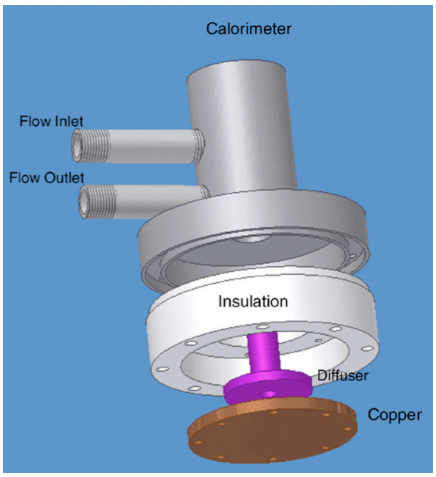

Figure 1.5 Flat-plate calorimeter schematic [8]

The cold-water calorimetery technique is verified experimentally by measuring the temperature of the copper receiving plate and calculating the radiative and convective heat losses, which are found to be 0.71% and 7.12% of the total power input, respectively. The convective losses are large enough that they should be accounted for. Including the thermal losses, an uncertainty of ±13% of the total energy input is associated with the flat-plate calorimeter measurements.

1.2 Objective

Calorimeters used today to measure concentrated solar energy have an uncertainty of ±0.5% to ±13% of the measured input, compared to an uncertainty of ±12% of the total flux measurement associated with the optical flux measurement method. A high accuracy is required when measuring the solar thermal power at the aperture of a reactor; thus, a water flow calorimeter is to be designed and fabricated to measure the concentrated solar radiation of the UMN solar simulator with an uncertainty less than ±12%. The calorimeter design will allow for varying power inputs and different aperture sizes, which will be accomplished with a removable aperture cover. Multiple covers can then be manufactured with different aperture diameters.

Chapter 2

Calorimeter Design

The main objective in designing the calorimeter is to accurately measure the amount of radiative power at the focal plane of the UMN solar simulator by minimizing the thermal losses to the ambient.

2.1 Calorimeter Selection

Two types of calorimeters are considered for the design: flat-plate and cavity (see Fig. 2.1(a) and (b)). Pérez-Rabago *et al.* [3] conducted experiments using a flat-plate calorimeter to measure the solar concentration power of a point focus concentrator and showed that the cold-water calorimetry technique cannot accurately be applied to high concentrated fluxes. The surface of the receiving plate cannot be maintained near ambient temperature and it degrades quickly. Therefore, for this study, a cavity calorimeter design is chosen and optimized to reduce thermal losses to the ambient.

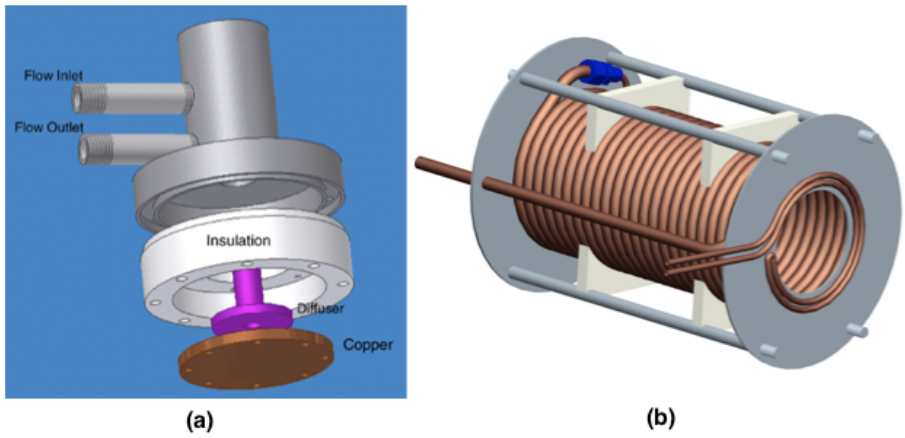

Figure 2.1 Schematics of the two types of calorimeters considered: (a) flat-plate [8] and (b) cavity

2.2 Geometrical Parameters

2.2.1 *Cavity*

To minimize reradiation losses, the cavity should approach that of a blackbody absorber, meaning the apparent emissivity of the cavity should approach one. This is accomplished by optimizing the cavity depth-to-radius ratio and the aperture radius-to-cavity radius ratio and by considering the surface emissivity of the cavity material [9]. Sparrow and Cess [10] determined that for cavities with diffusely reflecting walls there is a limiting case where an increase in the

cavity length will not further increase the apparent emissivity. As shown in Figure 2.2, a cavity depth-to-radius ratio (L/R) of four is the limiting case for all diffusely reflecting surface emissivities above 0.3.

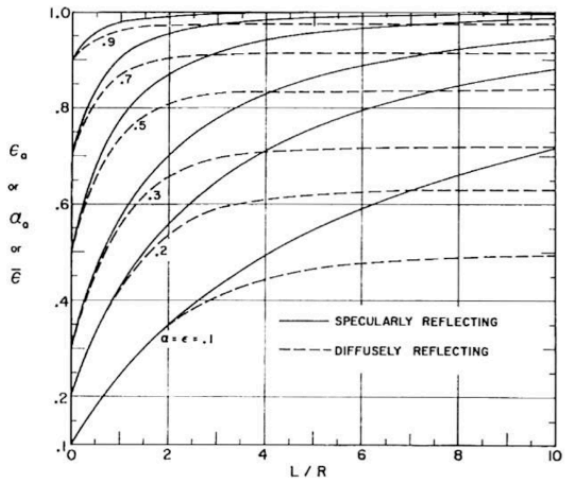

Figure 2.2 Apparent emittance for specularly and diffusely reflecting circular cylindrical cavities [10]

Figure 2.3 plots the data taken from Siegel and Howell [9] on apparent emissivity as a function of aperture radius-to-cavity radius ratio and surface emissivity. The cavity depth-to-radius ratio is four for all of the data points. An apparent emissivity of 0.98 or greater is desired to minimize reradiation effects, and it is assumed the material chosen for the cavity will have an emissivity of at least 0.5 when thermally oxidized. With that, and using Figure 2.3, an aperture radius-to-cavity radius ratio of 0.6 is used for an aperture diameter of 10 cm. The cavity length and radius can be determined from the ratios, and the parameters are given in Table 2.1. ε α

Table 2.1 Geometrical parameters

Dimension	Value	Unit
Cavity Length	30.48	cm
Cavity Radius	7.62	cm
Aperture Diameter	6, 10	cm

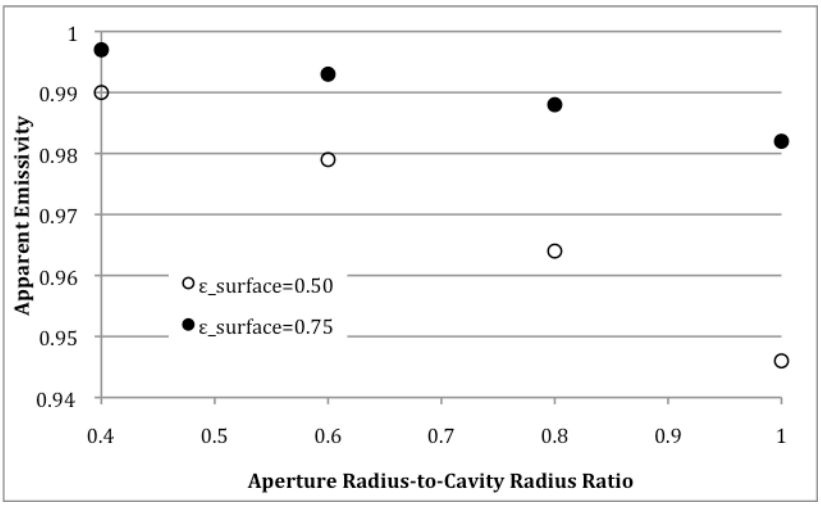

Figure 2.3 Apparent emissivity versus radii ratio

To minimize the thermal resistance between the inner surface of the cavity wall and the cooling fluid, the cavity wall is to be constructed using a tightly wound and soldered, helically coiled tube, as shown in Figure 2.4. The base of the cavity is comprised of a thin-walled base plate, with a lip along the circumference of the plate. This allows it to be partially inserted into the cavity wall and ensures the cavity is sealed off on the back end. Fluid flowing through a spirally coiled tube on the back of the plate removes the radiant energy incident on the plate. The spiral and helical tubes connect with a tube-tube fitting to allow constant fluid flow throughout the tube system. Figure 2.4 illustrates the whole cavity structure, and Figure 2.5 shows inner and outer cavity views of the base.

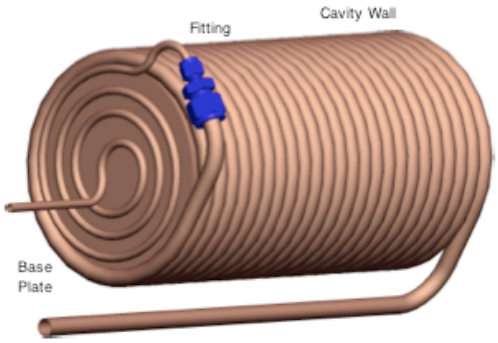

Figure 2.4 Cavity structure

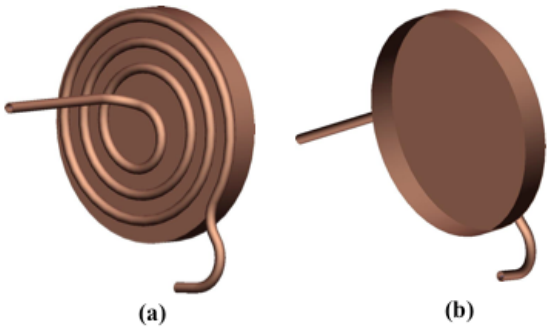

Figure 2.5: Base wall views: (a) outside cavity and (b) inside cavity

2.2.2 *Aperture Covers*

Figure 2.6 illustrates the aperture cover design. The aperture covers each have a spirally coiled tube soldered to the front face that is a separate cooling system from the cavity. This is to ensure the aperture cover does not get too hot; the aperture cover must be thermally separated from the cavity so that only radiant energy passing through the aperture is measured by the calorimeter.

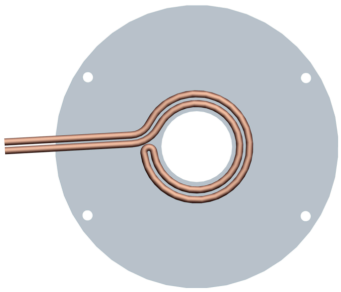

Figure 2.6 Aperture cover with cooling coil

To simplify the manufacturing process of the aperture covers, the acceptance angle of the solar simulator is accounted for without adding a bevel to the apertures' edges by using geometric relations. Knowing the desired diameter of the aperture, $D_{design,aperture}$, the thickness of the aperture cover, $t_{aperture\ cover}$, and the required acceptance angle, θ, simple trigonometry is used to determine what the actual diameter, $D_{cut,aperture}$, must be in order to allow the same amount of energy to pass through without a bevel. Figure 2.7 shows a schematic of this geometry. The increase in aperture size due removing the bevel is accounted for around the entire circumference. To simulate a 6 cm design diameter, a 6.368 cm actual diameter must be cut and for a 10 cm design diameter, the actual diameter must be 10.368 cm for a plate thickness of 2.38 mm.

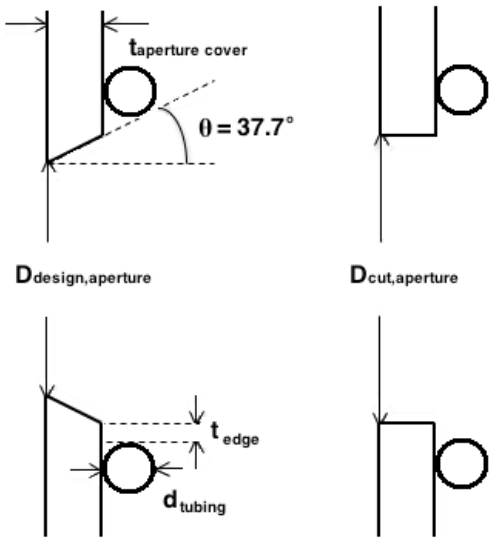

Figure 2.7 Schematic of geometry to account for acceptance angle on aperture covers

The acceptance angle on the aperture cover must also be accounted for when considering the location of the coiled tube in relation to the edge of the aperture; simulator rays within the acceptance angle cannot intersect with the tubing, as shown in Figure 2.7. Knowing the diameter of the tubing, d_{tubing} and the acceptance angle, trigonometry is used to calculate the minimum distance required from the edge of the aperture to the tube, t_{edge}, that will allow the desired radiant energy to pass through the aperture and not intersect with the cooling coil. As shown in Chapter 3, the majority of the energy that strikes the aperture is within a 3 cm radius from the aperture edge; therefore, the cooling coil should be placed as close as possible to the edge without interfering with the radiation passing through the aperture. It is calculated that the minimum distance from the aperture edge to the tube is 5 mm for the design.

2.3 Material Selection

The primary limitation in the design of the calorimeter is the materials selection for each part. Three parameters are considered when selecting calorimeter material: melting temperature, thermal conductivity, and emissivity. The material must be able to withstand the temperatures imposed on it when being irradiated. The cavity material must be highly conductive to allow for maximum heat transfer from the walls to the cooling fluid, and the support structure must have low conductivity to minimize heat transfer to the cavity. The cavity material must also have an emissivity greater than 0.5 when oxidized so that the apparent emissivity of the cavity is greater than 0.98 and reradiation is minimal.

2.3.1 *Cavity*

In addition to the above parameters, the cavity wall tubing must be compatible with water and capable of withstanding the pressure of the water flow. Three materials are evaluated for the cavity wall: aluminum alloy 3003, copper alloy 122, and stainless steel 304. Details of the material properties for the three metals are given in Table 2.2 [11, 12]. The aluminum alloy meets most of the design constraints; however, it does not have an emissivity that will ensure an apparent emissivity high enough to assume a blackbody cavity. While stainless steel has the highest emissivity, its low thermal conductivity will not provide sufficient heat transfer between the surface and the cooling fluid. The copper alloy meets all of the design parameters set for the helically coiled cavity wall; it conducts heat at a high rate, can withstand the temperatures the cavity walls will see while the cooling fluid is flowing, and has an emissivity greater than 0.5 when oxidized. The copper tubing is also compatible with water and can handle the pressure of the flow. Comparing the desired properties of each metal, copper alloy 122 tubing is to be used in the design of the helically coiled cavity wall. The design constraint for the spiral tubing on the back of the base wall is the same as for the cavity wall; therefore, it will also be made from copper alloy 122.

The design parameters for the base wall of the cavity are similar to the cavity wall parameters: high thermal conductivity, high melting temperature, and emissivity greater the 0.5. With that, an unpolished copper alloy 101 is chosen. The spiral copper tubing is to be soldered to the back face of the base wall.

Table 2.2 Material properties

Material	Thermal Conductivity at 25 °C ($Wm^{-2}K^{-1}$)	Melting Temperature (°C)	Emissivity at 25 °C, oxidized (-)	Max. Working Pressure at 25 °C (kPa)	Coefficient of Thermal Expansion (10^{-6} $m^1m^{-1}K^{-1}$)
Aluminum 3003	193	643	0.40	6895	22.2
Stainless Steel 304	18	1400-1450	0.85	11032	17.3
Copper 122	398	1083	0.78	4964	16.6
Copper 101	398	1083	0.78	--	16.6

2.3.2 *Aperture Covers*

The main design parameter for the aperture covers is to minimize heat transfer through the cover. The approach is to use a metal with low thermal conductivity and emissivity, and to keep its temperature low with the cooling system described in Section 2.2.2. With its low thermal conductivity (18 $Wm^{-2}K^{-1}$), stainless steel 304 is chosen for the aperture cover material. When polished, the emissivity of stainless steel is 0.16 [13]. The cooling tubes are to be made out of the same copper alloy 122 as the cavity wall tubing, and will be soldered to the stainless steel. As shown in Table 2.2, the coefficients of thermal expansion between copper 122 and stainless steel 304 are close enough that the two metals expanding at different rates from the heat is not a concern.

2.3.3 *Support Structure*

To ensure the cavity and aperture cover remain in the focal plane of the solar simulator a support system is designed around the cavity (see Fig. 2.8). The front plate of the structure is the aperture cover, while the back plate is a piece of stainless steel. The two plates are attached with four spacer rods, each containing a threaded rod to bolt the spacers in place. The cavity is held in place between the two plates with four supports made from calcium silicate insulation. The insulation is strong enough to support the cavity, and has a thermal conductivity of 0.08 $Wm^{-2}K^{-1}$ at room temperature [14], low enough to minimize heat transfer between the support structure and cavity. Fiberfrax Durablanket insulation is to be wrapped around the body of the cavity and behind the back of the cavity, secured using the spacer rods. This insulation has a thermal conductivity of 0.07 $Wm^{-2}K^{-1}$ at 200 °C [15], which decreases at lower temperatures; therefore, at room temperature, it will help to minimize the heat transfer from the cavity to the ambient.

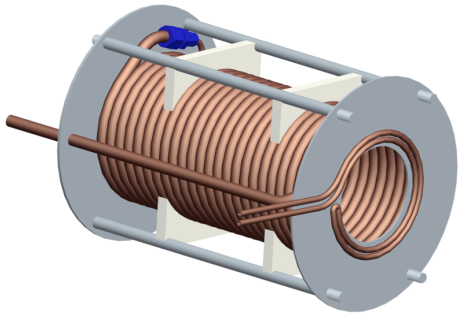

Figure 2.8 Support structure and cavity without insulation matting

2.4 Mass Flow Rate and Tubing Size Selection

The following parameters are considered when optimizing the mass flow rate of the cooling water inside the spiral and helical tubing. The temperature difference of the inlet and outlet fluid must be large enough to accurately measure with a thermopile. The mass flow rate of the water is set such that all of the input heat is absorbed, but the outlet temperature does not exceed 65°C. The mass flow rate must also be high enough that the Reynolds number associated with the pipe flow is at least 16,000, which corresponds to heat transfer coefficients in the spiral and helical tubing large enough to sufficiently remove the energy input; this analysis is presented in Chapter 4. Finally, the pressure drop through the system must be considered, so that a reasonably sized pump can be used to drive the water flow. The tubing diameter is to be a commercially available size to ease the manufacturing process.

Based on these parameters, equations (2.1) - (2.3) are used to choose a mass flow rate and determine an appropriate tubing size. The density, viscosity, and specific heat of the fluid are assumed to remain constant at 1,000 kgm^{-3}, 1.40E-6 m^2s^{-1}, and 4,204 $Jkg^{-2}°C^{-1}$, respectively, based on the inlet temperature. Two values of heat absorbed are considered: 3 kW, corresponding to the desired heat input into a thermochemical reactor, and 15.5 kW, associated with the maximum predicted power input as determined in Chapter 3. Type K and L copper, 0.64 cm (0.125 in) and 1.27 cm (0.375 in) tube sizes are considered because of their minimum bending radii (1.905 cm and 3.810 cm, respectively); spiral and helical coils are most easily manufactured using tubing of one of these sizes. Type K and L tubing are both made from copper alloy 122 and refer to different tube wall thicknesses. Table 2.3 summarizes the parameters based on the inner diameter and a range of mass flow rates.

$$\dot{m}_f = \rho_f \mathrm{v}_f \frac{\pi}{4} d_{i,tube}^2 \tag{2.1}$$

$$\mathrm{Re} = \frac{\mathrm{v}_f d_{i,tube}}{\nu_f} \tag{2.2}$$

$$q_{measured} = \dot{m}_f c_{p,f} \Delta T \tag{2.3}$$

Table 2.3: Summary of tube selection parameters

$\dot{m}_f$	0.10 (kgs^{-1})			0.12 (kgs^{-1})			0.14 (kgs^{-1})		
$d_{i,tube}$ (cm)	Re (10^3)	$T_{out,\ 3\ kW}$ (°C)	$T_{out,\ 15.5\ kW}$ (°C)	Re (10^3)	$T_{out,\ 3\ kW}$ (°C)	$T_{out,\ 15.5\ kW}$ (°C)	Re (10^3)	$T_{out,\ 3\ kW}$ (°C)	$T_{out,\ 15.5\ kW}$ (°C)
0.305	52	12.2	42.0	63	11.0	35.8	73	10.1	31.4
0.386	41	12.2	42.0	49	11.0	35.8	58	10.1	31.4
1.021	16	12.2	42.0	19	11.0	35.8	22	10.1	31.4
1.092	15	12.2	42.0	17	11.0	35.8	20	10.1	31.4

A mass flow rate of 0.12 kgs^{-1} is chosen for the design. A lower mass flow rate will not provide a sufficient heat transfer coefficient of the fluid in the helical tubing to adequately remove all of the input energy while maintaining a low enough cavity wall temperature. Larger mass flow rates result in a high pressure drop through the system that requires a 50 W (0.0671 hp) pump. The pressure drops through each section are presented in section 2.5. The temperature difference of the fluid is measurable for both energy inputs of 3 kW and 15.5 kW at a mass flow rate of 0.12 kgs^{-1}, and the outlet temperatures do not exceed 65°C. The burst strengths for annealed, type K and L copper tubing at the highest temperature in the design are an order of magnitude larger than the pressures being considered for the system [26], so this is not considered when selecting a tube size or mass flow rate.

The helical walls of the cavity are designed using 1.27 cm, type-L copper tubing, which corresponds to a 1.092 cm inner diameter. A larger tube size is used for the cavity walls to reduce the length of tubing required to build the cavity. 1.27 cm is small enough to have a sufficiently high heat transfer coefficient and will require substantially less tubing than 0.64 cm, easing the manufacturing process. For a helical cavity that is 30 cm in length and 15 cm in diameter, about 11 meters of nominal 1.27 cm tubing is required, compared to 22 meters of nominal 0.64 cm tubing, as calculated using equation (2.4). N is the number of turns in the helix, $d_{cl,h}$ is the centerline diameter of the helix, and P_h is the pitch, which is equal to the outer diameter of the tubing for this analysis.

$$L_h = \sqrt{\left(\pi d_{cl,h} N\right)^2 + \left(N P_h\right)^2} \tag{2.4}$$

Two design options are considered for the spiral tubing on the base of the cavity. The first option uses 0.914 m of 0.64 cm, type-L copper tubing, corresponding to a 0.386 cm inner diameter. Type-L tubing has the thinnest available wall, which reduces the resistance through the tube, and the small diameter allows for a small enough bending radius to adequately cover the

back plate of the cavity. The small inner diameter is also associated with a large enough heat transfer coefficient to absorb all of the energy incident on the base of the cavity, as shown in Chapter 4. The high velocity in the small spiral tubing causes a large pressure drop, and the head loss due to friction through the entire cavity is 31.9 m. The pressure drop analysis is presented in section 2.5.

The second design option for the spiral base uses 1.9 m of 1.27 cm, type-L copper tubing. This design allows for the helical wall and spiral base to be made from the same tubing, easing the manufacturing process and eliminating the pressure drop associated with cross-section expansion. The larger diameter results in a lower pressure drop through the spiral coil, and the head loss due to friction through the cavity is 9.0 m.

2.5 Estimating the Required Pump Size

To determine the pump size required to maintain the proper mass flow rate within the system, the total change in pressure between the inlet and outlet of the tubing is estimated using equation (2.5). The first term on the right-hand side gives the change in dynamic pressure, the second gives the change in pressure associated with a change in height, and the third gives the change in pressure associated with the head losses within the system.

$$\Delta p = \frac{\rho_f}{2}(\mathrm{v}_{\mathrm{outlet}}^2 - \mathrm{v}_{\mathrm{inlet}}^2) + \rho_f g \Delta z + \rho_f g \Sigma h_L \tag{2.5}$$

The first design option uses 0.64 cm tubing for the spiral cooling coil and 1.27 cm tubing for the helix. For this design, the change in dynamic pressure between the inlet and outlet of the system is associated with the change in cross-section of the tubing. Because the mass flow rate of the system remains constant, the fluid velocity changes, resulting in a pressure change of 103.5 kPa between the inlet and outlet.

The second design option uses 1.27 cm tubing for both the spiral and helical sections. Because the mass flow rate of the system remains constant, and the cross-sectional area of the inlet and outlet are the same, the change in dynamic pressure is zero. There is also no change in pressure associated with a change in height for either design, because the calorimeter is set up so that the inlet and outlet are at the same height.

The head loss through the cavity due to friction is considered separately for the spiral section and helical section because of the different geometries. To determine the change in the spiral section, a correlation for the Darcy-Weisbach friction factor for turbulent flow in a spiral tube is given by equation (2.6) [16]. The equivalent straight pipe friction factor, f_{straight}, is given by

the Haaland equation, (2.7). The tube is assumed to have a roughness, ε, of 0.0015 mm, which is a common value for copper tubing [17]. For the first design option, the straight pipe friction factor is found to be 0.0220, and the corresponding spiral friction factor is 0.0234. The straight pipe fraction factor is 0.0269 for the second design option, and the resulting spiral friction factor is 0.0304.

$$f_{spiral} = f_{straight} + 0.01\left(\frac{d_{i,tube}}{2r_o}\right)^{0.5}\left[\frac{1-(r_i/r_o)^{1.5}}{1-(r_i/r_o)^2}\right] \tag{2.6}$$

$$\frac{1}{\sqrt{f_{straight}}} = -1.8\log_{10}\left[\left(\frac{\varepsilon/d_{i,tube}}{3.7}\right)^{1.11} + \frac{6.9}{\mathrm{Re}}\right] \tag{2.7}$$

The pressure drop due to friction in the helical section is determined in a similar way as the spiral tube and is the same for both designs. Ito's correlation for the Darcy-Weisbach friction factor for turbulent flow in a helical coil is used, shown in equation (2.8), and cited by [18]. This correlation can be used when the Reynolds number of the flow is greater than or equal to the critical Reynolds number, $\mathrm{Re}_{crictical}$. The critical Reynolds number is 8,629, so the Ito correlation is appropriate to use for a mass flow rate of 0.12 kgs^{-1} and the design geometry, and the Darcy-Weisbach friction factor is found to be 0.1016.

$$f_{helix} = 0.304\,\mathrm{Re}^{-0.25} + 0.29\sqrt{\frac{d_{i,tube}}{d_{coil}}} \tag{2.8}$$

$$\mathrm{Re}_{critical} = 2{,}100\left(1 + 12\sqrt{\frac{d_{i,tube}}{d_{coil}}}\right) \tag{2.9}$$

With the friction factors calculated for the spiral and helical tubes, the pressure drop due to friction through each geometry is determined using equation (2.10) and the respective tube lengths and diameters. The fluid velocity, v_f, is defined as the volumetric flow rate over the cross-sectional wetted area of the tube. The pressure drop through the spiral tubing for the first design option is 291.9 kPa and 4.3 kPa for the second. The pressure drop through the helical tubing is 84.0 kPa.

$$\Delta p = f_{tube}\rho_f\left(\frac{L_{tube}}{d_{i,tube}}\right)\frac{v_f^2}{2} \tag{2.10}$$

For the first design option, an expansion in the tube diameter occurs where the spiral and helical coils connect. To account for the change in pressure associated with this expansion, the head loss due to the expansion is calculated using equation (2.11). The head loss due to sudden expansion is found to be 4.1 m.

$$h_{L,\text{expansion}} = \frac{(v_{inlet} - v_{outlet})^2}{2g} \tag{2.11}$$

The total change in pressure associated with the system is calculated by summing all of the pressure differences, and it is found to be 312.7 kPa for the first design option. To maintain a constant mass flow rate of 0.12 kgs^{-1} and account for the change in pressure, a pump that can supply 31.9 m of head must be used, from equation (2.12). The required minimum work input from the pump is found to be 37.5 W (0.0503 hp), using equation (2.13).

$$h_L = \frac{\Delta p}{\rho_f g} \tag{2.12}$$

$$\dot{W}_{pump} = \frac{\dot{m}\Delta p}{\rho_f} \tag{2.13}$$

For the second design option, the total change in pressure is calculated as 88.3 kPa, which corresponds to a pump that can supply 9.0 m of head. The required minimum work input from the pump is then found to be 10.6 W (0.0142 hp).

2.6 Final Design Selection

To summarize, a cavity calorimeter is designed to measure concentrated solar radiation. The body of the calorimeter is constructed using copper tubing and a copper plate, and the aperture cover is made from stainless steel with a cooling copper tube attached to its front face. Insulation surrounds the cavity to reduce heat transfer to the ambient. Appendix A gives a summary of the calorimeter components, as well as Pro/Engineer models for all parts.

The calorimeter measures the heat gain of water flowing through the system as radiant energy is passed through the aperture in the focal plane of the UMN solar simulator. Chilled water enters the inlet of the spiral tube at the center of the back plate, flows through the spiral and helical tubing, and exits at the outlet of the helical tube. The energy incident on the cavity surface is conducted through the helical tube and back plate and is then convected to the flowing water. The energy increase in the water can be observed by an increase in fluid temperature.

The temperature difference of the water between the inlet and outlet is measured using a thermopile. The mass flow rate of the water is held constant and measured using a flow meter. Knowing these values, the amount of energy output by the UMN solar simulator can be quantified.

Chapter 3

Predicted Power From Solar Simulator

A Monte Carlo ray tracing method is used to predict the amount of power that passes through the aperture of the calorimeter when it is placed in the focal plane of the UMN solar simulator. It is also used to predict the incident flux distribution on the cavity walls and aperture cover. The open-source code VeGas is used to implement the Monte Carlo ray tracing method [23]. To simulate the solar simulator output, the code developed in VeGas by Krueger that accurately defines the geometry and location of the seven power sources and reflectors is used [1].

3.1 Monte Carlo Ray Tracing Method in VeGas

The Monte Carlo ray tracing method simulates radiative energy exchange between surfaces. A large, finite number of discrete energy bundles, or rays, is emitted from a source, and each ray is then observed. The Monte Carlo method uses random sampling to determine the initial location, direction, and wavelength of a ray. The ray is tracked as it interacts with participating media and surfaces modeled in the system; these surfaces transmit, reflect, scatter, or absorb the ray. Intersection with a surface depends on the initial location and direction of the ray and on the location, geometry, and properties of the surface. If the system does not contain participating media, only reflection or absorption can occur. When a ray is reflected, its direction is recalculated and followed further; this process continues until it is either absorbed by a surface or exits the system. Each ray emitted at the source undergoes this process, and because of the randomness of the analysis, a large number of rays are used so that, statistically, the correct fractions are absorbed and reflected. The Monte Carlo program counts the number of rays that is absorbed by each surface, and this information is used to calculate the total energy absorbed. The Monte Carlo ray tracing method used to predict radiative transport described here is paraphrased from Modest [25].

The open-source code VeGas uses the Monte Carlo method to predict radiant energy exchange between user-defined surfaces and sources. Within the code, a number of assumptions have been made. It is assumed that the optical properties of the surfaces in the system are independent of wavelength (gray). It is also assumed that the surroundings are non-participating and that emission from the surface can be neglected, because the walls of the cavity are constantly cooled. The surfaces of the cavity and aperture cover are assumed to be diffuse and gray.

The Monte Carlo program for modeling the incident radiation from the solar simulator onto the calorimeter is explained as follows. Following a single ray, it is first launched from the source. A general geometric description of the ray is given by equation (3.1), where P_0 is the ray's point of origin, $\hat{u}$ is its directional unit vector, and P_1 is a point along the ray's path. The equation of the line for the ray's path from the origin to the point P_1 is given by equation (3.2), where D is the distance between points P_0 and P_1.

$$\left(P_1 - P_0\right) \times \hat{u} = 0 \tag{3.1}$$

$$P_1 - P_0 = D\hat{u} \tag{3.2}$$

These geometric equations for the ray and the geometric descriptions of the surfaces are used to determine if the ray intersects with a surface of the calorimeter. Equations (3.1) and (3.2) are solved simultaneously with the equations describing the calorimeter surface locations to determine an expression for D, which is then put back into equation (3.2) to find the point P_1. A ray is considered to have intersected a surface when P_1 is within the surface boundaries of the calorimeter. When a ray does intersect a surface, it will either reflect off of the surface or be absorbed by it, determined by equation (3.3). $\Re_\rho$ is a random number generated by the program, and ρ is the reflectivity of the surface. If equation (3.3) is satisfied, the ray is reflected and its path is followed until it intersects with another surface or leaves the system.

$$\Re_\rho \le \rho \tag{3.3}$$

If equation (3.3) is not satisfied, the ray is absorbed by the surface element, and the ray counter associated with the surface element is increased by one. The above procedure occurs for all of the rays emitted by the sources. After all of the rays are accounted for, equation (3.4) is used to calculate the total energy absorbed by each surface element, q_j", where N_j is the number of rays intercepted by the surface element with area A_j, and q_{ray} is the power associated with each ray.

$$q_j" = \frac{\int_{A_j} q" \, dA}{A_j} \approx \frac{N_j q_{ray}}{A_j} \tag{3.4}$$

The total power absorbed by each calorimeter surface is calculated by summing the power at every surface element.

3.2 Model of Solar Simulator

The solar simulator is modeled using the geometric relations derived by Krueger [1]. The xenon arc lamps are modeled as cylindrical sources that are 2.0 mm in radius and 6.3 mm long

and emit radiation diffusely from the volume. The Monte Carlo simulation uses $N_{ray} = 10^7$ rays per lamp, and the total amount of energy emitted by the lamp is divided equally by the number of rays, so that each ray carries the same amount of energy. The inner surfaces of the reflectors surrounding each lamp are modeled as truncated ellipsoids of revolution. They have a reflectivity of $\rho = 0.9$ and are assumed to have specular reflectance with specular error that accounts for surface quality variance in the manufacturing process.

Table 3.1: Coordinates of the arc center and foot points of the ellipsoid and cylindrical arc in the global system centered at the simulator focal point [1]

	Arc center coordinates (m)			**Ellipsoid *F* coordinates (m)**			**Arc *F* coordinates (m)**		
Unit	x	y	z	x	y	z	x	y	z
1	-1.8260	0.4453	0.7713	-0.9130	0.2227	0.3856	-1.8288	0.4460	0.7725
2	-1.8260	0.4453	-0.7713	-0.9130	0.2227	-0.3856	-1.8288	0.4460	-0.7725
3	-1.8260	0.0000	0.8906	-0.9130	0.0000	0.4453	-1.8288	0.0000	0.8920
4	-2.0316	0.0000	0.0000	-1.0158	0.0000	0.0000	-2.0347	0.0000	0.0000
5	-1.8260	0.0000	-0.8906	-0.9130	0.0000	-0.4453	-1.8288	0.0000	-0.8920
6	-1.8260	-0.4453	0.7713	-0.9130	-0.2227	0.3856	-1.8288	-0.4460	0.7725
7	-1.8260	-0.4453	-0.7713	-0.9130	-0.2227	-0.3856	-1.8288	-0.4460	-0.7725

Table 3.1 is taken from Krueger and defines the coordinates of the seven arc lamp sources and their corresponding reflector ellipsoids in a global Cartesian coordinate system, with the focal point of the simulator at the origin. The foot-point, *F*, of each cylindrical source defines the point at the end of the cylinder with a radius of zero, and the directional vector, **v**, defines the orientation of the cylinder (see Fig 3.1). The length of the cylinder, L, and the radius, R, are defined in the VeGas code. Each truncated ellipsoid, used to model the reflectors, is defined by a foot-point at the center of a completed ellipsoid and a directional vector, **v**, as shown in Figure 3.2. The derivation of these geometric relations is discussed in greater detail in Krueger [1].

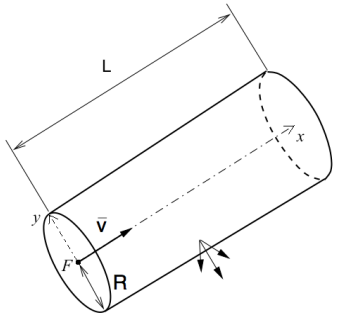

Figure 3.1 Schematic of cylindrical source, with defining length L, radius R, and directional vector v [24]

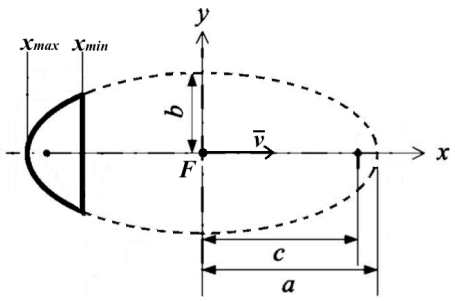

Figure 3.2 Schematic of a two-dimensional ellipse, to be rotated about the x-axis to form a three-dimensional ellipsoidal reflector [1]

The center of a cylindrical source is located at the ellipsoid's focal point within each truncated ellipsoid, so that the majority of the energy emitted from a source is reflected to the ellipsoid's opposite focal point. The reflectors are oriented such that all seven have a common opposite focal point, which is where the calorimeter's aperture is located. When the stochastic rays are launched from each power source, they are tracked. The rays are followed as they are either lost to space or intercepted by the reflector surface, and those that hit the reflector surface are either reflected or absorbed. The majority of the rays that are reflected reach the focus plane and are intercepted by the calorimeter surfaces; these interactions are discussed in detail in Section 3.3.

3.3 Model of Calorimeter

The calorimeter surfaces considered in the analysis are modeled using cylinders and rings, as shown in Figure 3.3. The inner surface of the cavity is comprised of a cylindrical body and a ring for the back wall. The front of the cavity is a plate, which encompasses the aperture. It is modeled by rings for the front and back surfaces and a cylinder for the edge around the aperture. The global origin, o, is located at the focal point of the simulator and in the center of the aperture, as shown in Figure 3.3.

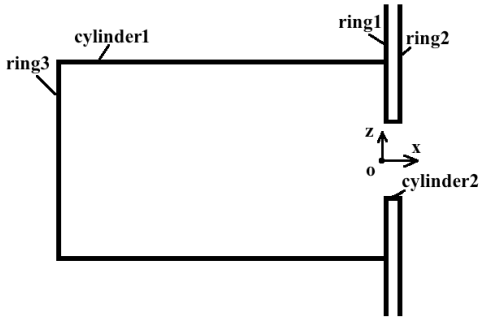

Figure 3.3 Schematic of modeled calorimeter surfaces

Figures 3.4 and 3.5 show schematics taken from Petrasch [23] of the cylinder and ring geometries. Each surface is discretized by a set grid number, defined in the VeGas code. For this analysis, a fine grid is used to attain a more accurate flux distribution throughout the cavity. The cavity surfaces are made from copper and defined to have an emissivity of 0.78, which accounts for an oxidation layer across the metal. The aperture surfaces are made from stainless steel and assigned an emissivity of 0.63. A physical attribute of the calorimeter that is not accounted for in the Monte Carlo simulation is that the surface of the cavity wall is made of a coiled tube. There is currently no feasible way to model such geometry in VeGas; therefore, it is assumed the surface is smooth. Such an approximation is acceptable, because adding the curvature of the tubes will only result in an increase in the apparent absorptivity of the cavity. The normal vector for every surface is defined by **n** = (1.0, 0.0, 0.0). Table 3.2 defines the coordinates of the calorimeter surfaces based off the global origin for a 6 cm diameter aperture. The coordinates for a 10 cm diameter aperture are presented in Appendix B.

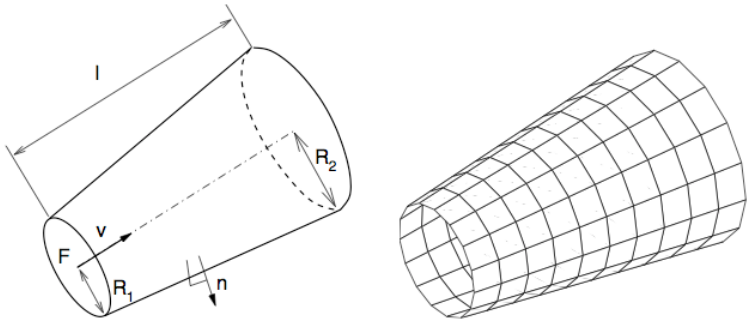

Figure 3.4 Schematic of cylinder, with defining length l, radii R_1 and R_2, normal vector n, and directional vector v. Schematic of discretized cylinder [24]

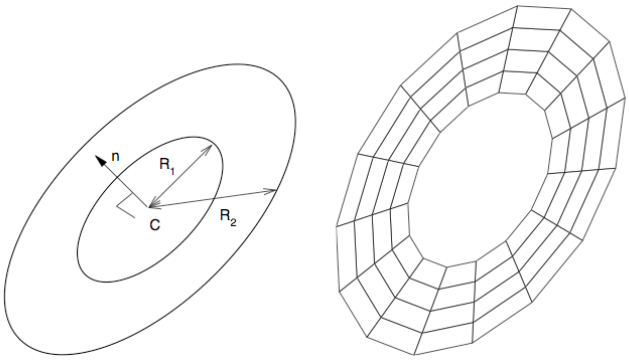

Figure 3.5 Schematic of ring, with defining radii R_1 and R_2, center C, and normal vector n. Schematic of discretized ring [24].

Table 3.2: Coordinates of the center and foot points of the cavity and aperture surfaces in the global system centered at the simulator focal point for 6 cm diameter aperture

	Center/foot-point coordinates (m)			Radii (m)		Length (m)
Surface	x	y	z	R_1	R_2	l
Ring 1	0.00000	0.00000	0.00000	0.03184	0.12600	--
Ring 2	0.01900	0.00000	0.00000	0.03184	0.12600	--
Ring 3	-0.30000	0.00000	0.00000	0.00000	0.07000	--
Cylinder 1	-0.30000	0.00000	0.00000	0.07000	0.07000	0.30000
Cylinder 2	0.00000	0.00000	0.00000	0.03184	0.03184	0.00238

3.4 Determining the Power of Each Radiation Source

In order to define the thermal power emitted from each source in the VeGas code, experimental solar simulator data from Krueger *et al.* [2] is used to extrapolate the electrical-to-thermal efficiencies. Table 3.3 summarizes the data taken from Krueger *et al.* The measured amperage and voltage of each lamp is given; from these data, the electrical input power for each lamp is calculated. The average flux over a 6 and 10 cm area in the focal plane of the simulator, measured using the Lambertian target and CCD camera technique described in Chapter 1, is also presented for each lamp. The average power is calculated by multiplying the measured average flux by the appropriate area.

Table 3.3: Summary of electrical and thermal power for individual solar simulator lamps

		Measured thermal power, $P_{incident,measured}$ (W)	
Unit	**Electrical input power to lamp, $P_{electrical}$ (W)**	6 cm target	10 cm target
1	5659.50	1205.47	1737.47
2	4950.00	1331.55	1811.70
3	5270.00	1217.37	1760.18
4	5145.00	1378.86	1924.23
5	5025.00	1195.95	1638.15
6	4995.00	1348.65	1823.18
7	4950.00	1287.00	1806.75

To define the thermal output power ($P_{thermal,i}$) of each source, i, in the VeGas code, the electrical efficiency of each lamp must be determined, as defined by equation (3.5). The measured thermal power of each lamp at the focal plane, given in Table 3.3, is not equal to the

thermal output of each lamp. These values include the transfer efficiency between the lamp and focal plane, as well as the electrical efficiency. The VeGas simulation accounts for a theoretical transfer efficiency by allowing rays to be lost to space, so using the values in the table will cause the transfer efficiency to be accounted for twice and result in a predicted flux that is too low. To determine the electrical efficiency from the given data, the transfer efficiency of the solar simulator must be estimated. A Monte Carlo simulation is run assuming all of the electrical input power of each lamp is emitted as thermal power. The predicted power incident on a 10 cm target in the focal plane of the solar simulator for each lamp is recorded, and the corresponding transfer efficiencies are calculated using equation (3.6), where $P_{incident,model,i}$ is the corresponding power incident on the target.

$$\eta_{electrical,i} = \frac{P_{thermal,i}}{P_{electrical,i}} \tag{3.5}$$

$$\eta_{transfer,i} = \frac{P_{incident,model,i}}{P_{electrical,i}} \tag{3.6}$$

The amount of thermal power lost to space is also calculated using equation (3.7). An assumption is made that the same amount of power is lost to space for a given lamp, regardless of its thermal output power. With this assumption, the sum of the measured thermal power incident on the target ($P_{incident,measured}$) from Table 3.3 and the thermal power lost to space will give the amount of thermal power emitted from each source, allowing the electrical efficiency of each source to be calculated by equation (3.5). The VeGas code also requires the relative strength of each source. This is determined by equation (3.8), where S_i is the relative strength, $P_{thermal,total}$ is the total thermal power of the solar simulator, and $P_{thermal,i}$ is the thermal power emitted by the corresponding source. Table 3.4 summarizes the results of the above calculations for each lamp.

$$P_{lost,i} = P_{electrical,i} - P_{incident,model,i} \tag{3.7}$$

$$S_i = \frac{P_{thermal,i}}{\sum_{i=1}^{7} P_{thermal,i}} \tag{3.8}$$

Table 3.4: Summary of electrical efficiency and relative strength for each lamp

Unit	$P_{incident}$ (W)	$\eta_{transfer}$ (%)	P_{lost} (W)	$P_{thermal}$ (W)	$\eta_{electrical}$ (%)	S (%)
1	3552.41	62.77	2107.01	3844.48	67.93	14.84
2	3107.73	62.78	1842.27	3653.97	73.82	14.11
3	3307.87	62.77	1962.13	3722.31	70.63	14.37
4	3230.59	62.79	1914.41	3838.64	74.61	14.82
5	3154.56	62.78	1870.44	3508.59	69.82	13.55
6	3134.64	62.76	1860.36	3683.54	73.74	14.22
7	3108.17	62.79	1841.83	3648.58	73.71	14.09

Using the calculated thermal power for each source in the VeGas code, the program over-predicts the incident thermal power an average of 400 W per lamp compared to the measured incident power from [2]. This discrepancy is small compared to the overall output of the solar simulator, so the predicted values of the Monte Carlo program are used in the heat transfer analysis to estimate the thermal losses of the system in Chapter 4.

3.5 Monte Carlo Simulation Results

With all of the parameters defined in the VeGas code, Monte Carlo simulations of the solar simulator are run for both a 6 and 10 cm diameter aperture, and the incident flux distribution from the simulator on each surface of the calorimeter is modeled. Figures 3.6-10 illustrate the results for a 6 cm diameter aperture. Note that the length scale and flux scale for each flux map are different.

Because copper is a highly absorptive material, the majority of the rays that intersect with the cavity walls are absorbed. As illustrated in Figures 3.6 and 3.7, the lamps create six regions of high intensity flux symmetrically around the cylindrical cavity wall and one region on the back wall of the cavity. This results in seven local “hot spots”. A simple one-dimensional heat transfer analysis is done to verify that the temperature of the wall at these locations will not surpass the melting temperature of copper while chilled water is flowing through the tubing. This assessment is completed in Chapter 4.

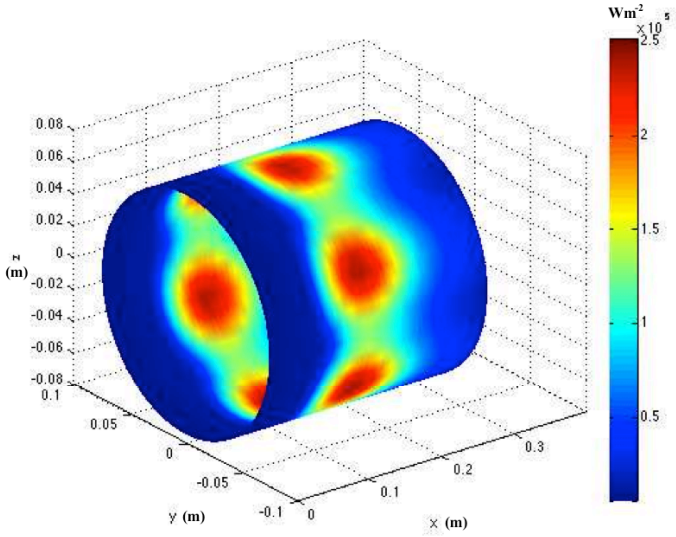

Figure 3.6 Flux distribution on cavity wall with 6 cm diameter aperture

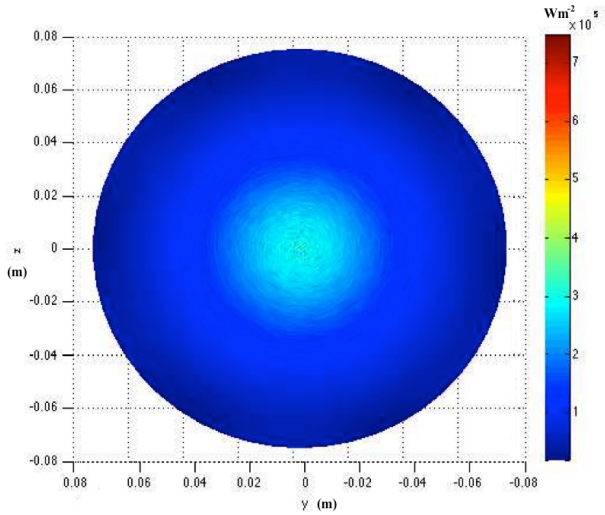

Figure 3.7 Flux distribution on cavity back wall with 6 cm diameter aperture

Figure 3.8 illustrates the flux distribution on a 6 cm diameter aperture cover. This flux map is used to determine the geometry and location of the cooling coil on the cover. The only part of the cover that sees high intensity flux is a 2 cm radius section around the aperture. This area requires a cooling coil so that the material does not surpass its melting temperature and so that the cover emits a negligible amount of energy into the cavity. Heat transfer calculations are presented in Chapter 4.

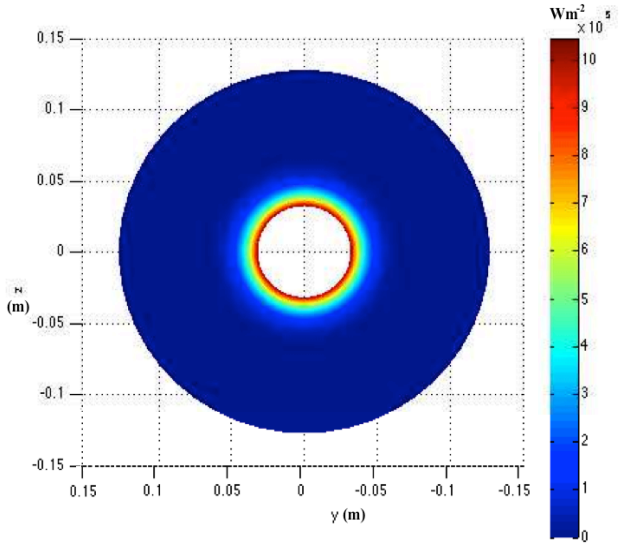

Figure 3.8 Flux distribution of aperture cover surface facing simulator with 6 cm diameter aperture

The flux distributions on the surface of the aperture cover facing into the cavity and on the edge of the 6 cm diameter aperture are shown in Figures 3.9 and 3.10. The inner surface of the aperture cover has a low flux distribution due to the relatively low reflectivity of the cavity material and the geometry of the cavity. The cavity is designed so that majority of the reflections intersect with itself, not the aperture cover. The chilled water inside the cooling coil on the cover will absorb majority of the energy seen by the aperture edge.

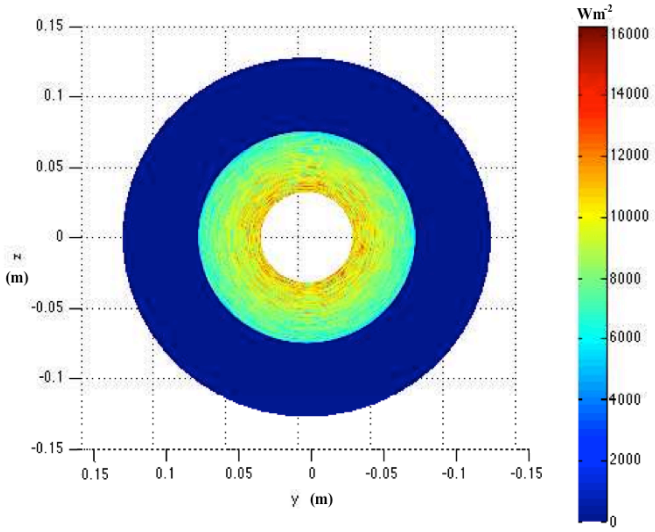

Figure 3.9 Flux distribution of aperture cover surface facing into cavity with 6 cm diameter aperture

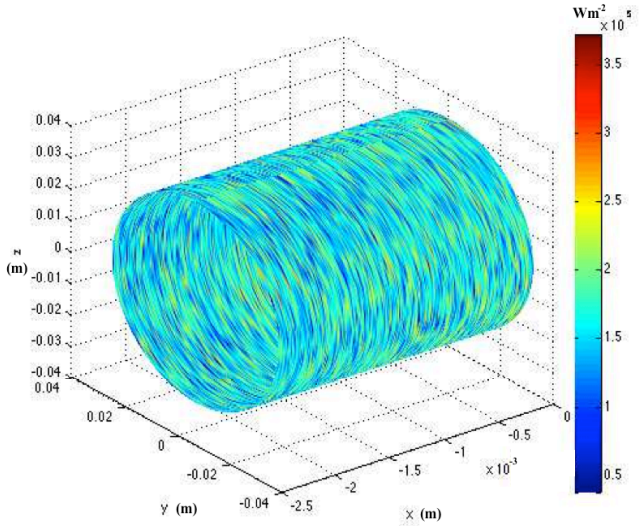

Figure 3.10 Flux distribution on aperture edge with 6 cm diameter aperture

The incident power over each surface is calculated by integrating the flux over the corresponding surface area. Table 3.5 summarizes the results of this analysis. As expected, more power is incident on the cavity surfaces for a 10 cm diameter aperture than for a 6 cm diameter aperture. The amount of power incident on the aperture cover reduces by a factor of ten when increasing the aperture size from 6 cm to 10 cm. This result is due to the fact that majority of the power on the plate with a 6 cm diameter aperture is incident within a 2 cm radius of the aperture. Increasing the aperture diameter to 10 cm eliminates that area, and the energy passes into the cavity, causing the amount of power on the cavity surfaces to increase. The predicted power on the surfaces of the cavity is used in the heat transfer analysis to estimate the thermal losses of the system in Chapter 4.

Table 3.5: Summary of predicted incident power using Monte Carlo method

	Power incident on cylindrical wall surface (W)		**Power incident on base wall surface (W)**		**Power incident on aperture cover surfaces (W)**		**Power incident on back aperture surface (W)**	
Unit	6 cm	10 cm	6 cm	10 cm	6 cm	10 cm	6 cm	10 cm
1	1,721	2,262	30	42	334.17	33.63	18.14	13.50
2	1,636	2,150	29	40	317.15	40.12	17.19	12.92
3	1,666	2,190	29	41	323.37	40.86	17.65	13.18
4	426	555	1,421	1,789	279.13	21.77	12.84	9.30
5	1,571	2,065	28	28	304.85	30.60	16.46	12.30
6	1,649	2,167	29	29	320.08	32.30	17.37	12.95
7	1,634	2,147	29	29	316.95	31.81	17.39	12.81
All	10.303	13,536	1,594	2,032	2,195.70	214.62	117.03	86.96

3.6 Summary

A Monte Carlo ray tracing method is used to predict the radiative transport between the UMN solar simulator and a calorimeter in its focal plane. The simulator geometry is taken from Krueger *et al.* The xenon arc lamps are modeled as cylindrical rods, each centered at the focal point of a truncated ellipsoid acting as a reflector. The calorimeter is modeled using cylinders and rings, with the aperture in the focal plane of the simulator. The air is non-participating. The model predicts the incident flux distribution on the surfaces of the calorimeter and is used to verify that any local "hot spots" will not surpass the melting temperature of copper; this is completed in Chapter 4. The corresponding power measurements are used in the heat transfer analysis in Chapter 4 to estimate thermal losses from the calorimeter to the ambient.

Chapter 4

Heat Transfer Analysis

The thermal losses of the system are estimated by carrying out an energy balance on the calorimeter. If the losses are small enough, it is reasonable to assume majority of radiant energy from the solar simulator is being measured by the calorimeter. The thermal loss estimation is incorporated into the uncertainty analysis to determine the accuracy of the calorimeter. The maximum possible surface temperatures of the cavity walls and aperture cover can be calculated to ensure thermal losses are minimized and the melting temperatures of the materials are not surpassed. The radiant energy incident upon the cavity surface is conducted through the helical tube and back plate and is then convected to the fluid flowing through the tubes. The energy increase in the fluid can be observed by an increase in fluid temperature. The following analyses were coded in MATLAB and evaluated for varying power inputs. It is shown that the thermal losses of the system to the ambient account for only 1% of the total input.

4.1 Calorimeter Energy Balance

A steady state energy balance on the system is illustrated in Figure 4.1 and described by equation (4.1). The radiant energy that is passed through the aperture, q_{in}, is balanced by the heat lost to the fluid by forced convection, $q_{conv,f}$, the energy lost due to reflection through the aperture, q_{ref}, reradiation through the aperture, q_{rerad}, and natural convection through the aperture, $q_{conv,i}$. For the analysis, it is assumed that the cavity is insulated well enough so that convective losses outside the calorimeter are zero.

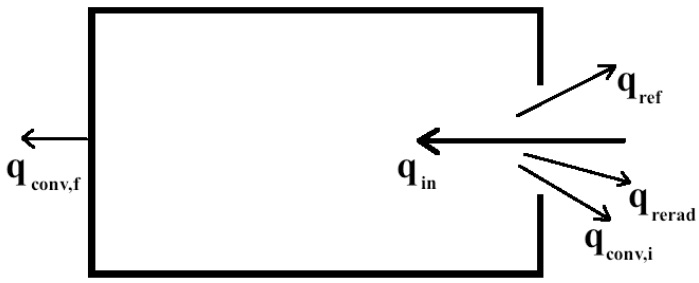

Figure 4.1 Schematic of energy balance on calorimeter

$$q_{in} = q_{conv,f} + q_{ref} + q_{rerad} + q_{conv,i} \tag{4.1}$$

The total amount of energy convected to the cooling fluid, $q_{conv,f}$, is described by equation (4.2), where $q_{conv,f,bw}$, and $q_{conv,f,cw}$ are the amounts of energy convected to the fluid flowing

through the spiral and helical tubing, respectively. These values are also equal to the change in energy of the fluid flowing through the respective tubing and are quantified by equations (4.3) and (4.4). The overall heat transfer coefficient-area product *(UA)* is defined by the heat transfer surface, so because the base of the cavity has a different geometry than the cylindrical wall, the two surfaces have different *UA* values and are evaluated separately.

$$q_{conv,f} = q_{conv,f,bw} + q_{conv,f,cw} \tag{4.2}$$

$$q_{conv,f,bw} = \dot{m}_f c_{p,f} (T_{bw,out,f} - T_{bw,in,f}) = (UA)_{bw} (T_{bw} - T_{b,f,bw}) \tag{4.3}$$

$$q_{conv,f,cw} = \dot{m}_f c_{p,f} (T_{cw,out,f} - T_{cw,in,f}) = (UA)_{cw} (T_{cw} - T_{b,f,cw}) \tag{4.4}$$

T_{bw} is the base wall temperature, T_{cw} is the cylindrical wall temperature, $T_{b,f,bw}$ is the bulk temperature of the water in the spiral tubing, and $T_{b,f,cw}$ is the bulk temperature of the water in the helical tubing. The temperatures of the cavity base wall and cylindrical wall are solved for iteratively, using equations (4.1) and (4.2). Knowing the wall temperatures, the thermal losses of the system can be determined and added to the overall uncertainty of the calorimeter measurement, as shown in section 4.5.

From the Monte Carlo simulation, 14% of the energy input into the calorimeter is incident on the back wall of the cavity and 86% is incident on the cylindrical wall. The first iteration of the program assumes all of the energy incident on each surface is convected to the fluid flowing across that surface, as shown by equations (4.5) and (4.6).

$$0.14 q_{in} = q_{conv,f,bw} \tag{4.5}$$

$$0.86 q_{in} = q_{conv,f,cw} \tag{4.6}$$

The outlet temperatures of the fluid through each tube configuration are found using equations (4.3), (4.4), (4.5), and (4.6). The bulk fluid temperatures of the water in the spiral tubing and helical tubing are then solved for using equations (4.7) and (4.8). It is assumed the inlet temperature of the fluid in the helical tube is equal to the outlet temperature of the fluid in the spiral tube.

$$T_{b,f,bw} = \frac{T_{bw,in,f} + T_{bw,out,f}}{2} \tag{4.7}$$

$$T_{b,f,cw} = \frac{T_{cw,in,f} + T_{cw,out,f}}{2} \tag{4.8}$$

The temperatures of the base wall and cylindrical wall are then determined using the bulk fluid temperatures and equations (4.3) and (4.4). The two wall temperatures are area-averaged to give a weighted wall temperature (equation (4.9)), which is used to calculate the convection,

reflection, and reradiation losses through the aperture. All of the thermal losses are defined in section 4.2. These losses are subtracted from the total amount of energy input into the cavity (equation (4.10)), and this gives a new value for the total amount of energy convected to the fluid.

$$T_{w,avg} = \frac{T_{cw}A_{cw} + T_{bw}A_{bw}}{A_{cw} + A_{bw}} \tag{4.9}$$

$$q_{new,conv,f} = q_{in} - q_{conv,i} - q_{ref} - q_{rerad} \tag{4.10}$$

The value is area-averaged to estimate the amount of energy convected to the fluid flowing across the base wall and cylindrical wall, individually, as shown by equations (4.11) and (4.12). The program then repeats, using the new measured values to solve for the fluid outlet temperatures in equations (4.3) and (4.4).

$$q_{conv,f,bw} = q_{new,conv,f}\,\frac{A_{bw}}{A_{cw} + A_{bw}} \tag{4.11}$$

$$q_{conv,f,cw} = q_{new,conv,f}\,\frac{A_{cw}}{A_{cw} + A_{bw}} \tag{4.12}$$

The program converges when the sum of the thermal losses and the energy convected to the fluid is equal to the energy input into the system and when the respective wall temperatures in each equation are the same. A flowchart of the iteration is given in Appendix D.

It is also important to consider the energy on the surface of the aperture cover facing into the cavity. Because this energy passed through the aperture, it should be accounted for; however, the chilled water does not measure the incident energy on the back surface of the aperture cover. Therefore, it is important that the power incident on this surface be as small as possible. For all seven lamps on, 117 W is incident on the back surface of the 6 cm diameter aperture cover and 87 W is incident on the back surface of the 10 cm diameter aperture cover. These losses account for less than 1% of the total energy that passes into the cavity for both aperture sizes and is, therefore, neglected.

4.2 Thermal Loss Analysis of Cavity

4.2.1 *Forced Convection to Cooling Fluid*

The total amount of energy convected to the cooling fluid, $q_{conv,f}$, described by equations (4.2), (4.3) and (4.4) is calculated as follows. Figure 4.2 shows the resistance networks for the two surfaces, and equations (4.13) and (4.14) define $(UA)_{bw}$ and $(UA)_{cw}$, respectively. The terms in the denominators represent the resistance due to conduction through the tubing ($R_{cond,s}$ and

$R_{cond,h}$) , base plate ($R_{cond,bp}$), and solder ($R_{cond,sol}$) and the resistance due to convection of the chilled water ($R_{conv,s}$ and $R_{conv,h}$).

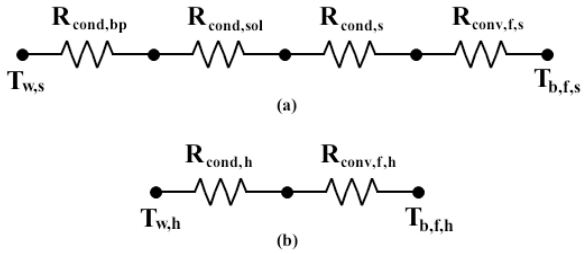

Figure 4.2 Resistance network for (a) base of cavity and (b) cylindrical wall

$$(UA)_{bw} = \frac{1}{\mathrm{R}_{cond,bp} + \mathrm{R}_{cond,sol} + \mathrm{R}_{cond,s} + \mathrm{R}_{conv,f,s}} = \frac{1}{\frac{t_{bp}}{A_{bp}k_{Cu}} + \frac{t_{sol}}{A_{sol}k_{sol}} + \frac{\ln(r_{o,s}/r_{i,s})}{2\pi L_s k_{Cu}} + \frac{1}{A_s h_s}} \tag{4.13}$$

$$(UA)_{cw} = \frac{1}{\mathrm{R}_{cond,h} + \mathrm{R}_{conv,f,h}} = \frac{1}{\frac{\ln(r_{o,h}/r_{i,h})}{2\pi L_h k_{Cu}} + \frac{1}{A_h h_h}} \tag{4.14}$$

The heat transfer coefficients of fluid flowing through the spiral and helical tubing configurations are determined using equation (4.16) and the Nusselt number correlations presented in equations (4.17) and (4.18). The Nusselt correlation for a heated spiral tube was developed for turbulent, fully-developed flow with $\mathrm{Pr} \geq 5$ and $300 \leq \mathrm{Re}(2r_{i,s}/d_{avg,s})^{0.5} \leq 2200$ [19], where Re is the Reynolds number of the flow given by equation (4.15), and is given by equation (4.17). The Nusselt correlation for a horizontal, helical coil with a uniform heat flux boundary condition for turbulent and fully-developed flow with $5{,}000 < \mathrm{Re} < 100{,}000$, $0.7 < \mathrm{Pr} < 5$, and $0.0267 < d_i/d_{cl,h} < 0.0884$ [20] is given by equation (4.18).

$$\mathrm{Re} = \frac{\mathrm{v}_f d_{i,t}}{\nu_f} \tag{4.15}$$

$$Nu = \frac{h_f d_{i,t}}{k_f} \tag{4.16}$$

$$Nu_s = 27.358\left[\mathrm{Re}_s\left(\frac{2r_{i,s}}{d_{avg,s}}\right)^{0.5}\right]^{0.287} \mathrm{Pr}_f^{-0.949} \tag{4.17}$$

$$Nu_h = 0.00619\,\mathrm{Re}_h^{0.92}\,\mathrm{Pr}_f^{0.4}\left(1 + 3.455\frac{2r_{i,h}}{d_{cl,h}}\right) \tag{4.18}$$

The heat transfer areas for convection by the fluid, A_s and A_h in equations (4.13) and (4.14), are approximated as the inner surface area of the respective tubing. The full circumference

of the tubing is not being struck with incident radiation; however, this assumption is valid because the resistance due to convection through the fluid is much larger than the resistance due to conduction through the copper tubing. The heat will conduct across the tube wall before the fluid, resulting in a uniform temperature distribution around the circumference of the tube wall.

4.2.2 *Reflection and Reradiation Losses*

As described in Chapter 2, the cavity approaches that of a blackbody absorber because of its geometrical parameters. With that, q_{ref} is minimized and calculated by equation (4.19). The amount of energy reflected out of the cavity is estimated by multiplying the energy that passes into the cavity by the apparent reflectivity of the cavity. The surface is assumed gray; therefore, the emission and absorption of radiation at the surface is assumed to be the same. Also, because the surface is opaque, the reflectivity and absorptivity sum to one; therefore, the apparent reflectivity of the cavity can be equated to one minus its apparent emissivity.

$$q_{ref} = q_{in}(1-\varepsilon_a) \tag{4.19}$$

Reradiation losses through the aperture are a function of the aperture area, apparent emissivity of the cavity, and the surface temperature of the cavity walls, as described by equation (4.20). The surface temperature of the wall, $T_{w,avg,}$ is the area-averaged temperature of the base plate temperature, $T_{w,s}$, and cylindrical wall temperature, $T_{w,h}$. The apparent emissivity, ε_a, is the ratio of radiant energy leaving the cavity to the radiant energy emitted by a blackbody at the same temperature and area as the aperture. As described in Chapter 2, correlations are available for cylindrical cavities with apertures that relate apparent emissivity to different cavity length-to-radius ratios and aperture radius-to-cavity radius ratios. Given the dimensions of the cavity, one can use these correlations to estimate an apparent emissivity of 0.99 for the cavity.

$$q_{rerad} \approx A_{ap}\varepsilon_a \sigma T_{w,avg}^4 \tag{4.20}$$

4.2.3 *Natural Convection Inside Cavity*

Thermal loss due to natural convection inside the cavity is defined by equation (4.21). The heat transfer coefficient, h_i, is defined using the Nusselt number correlation for natural convection inside a horizontal, heated cavity, given by equation (4.22) [21]. L_{ch} is an experimentally determined characteristic length that incorporates the length of the cavity and diameters of the cavity and aperture into a single length, as shown in equation (4.23). All of the properties of air are evaluated at ambient, because the change in temperature between the average

wall temperature and ambient is small enough that the property values of air do not change significantly.

$$q_{conv,i} = h_i A_{cav} (T_{w,avg} - T_{amb}) \tag{4.21}$$

$$Nu_{L_{ch}} = 0.0196 Ra_{L_{ch}}^{0.41} \Pr_{air}^{0.13} \tag{4.22}$$

$$L_{ch} = [4.08\cos(-0.11)^{5.41} d_{cav}] + [-1.17\cos(-0.30)^{7.17} L_{cav}] + [0.07\cos(-0.08)^{1.99} d_{ap}] \tag{4.23}$$

4.2.4 *Solving for the Thermal Losses*

The wall temperatures for a 6 cm diameter aperture and all seven lamps turned on are found to be 18.6 °C for the base of the cavity and 20.3 °C for the cylindrical wall. Ambient temperature is assumed to be 20 °C, and the wall temperatures are close to ambient because the energy incident on the walls is quickly convected to the chilled water, which enters the system at 5 °C and exits the coil at 23 °C. Table 4.1 summarizes the thermal losses of the system for this case. Majority of the energy is lost to the fluid, and only 93 W (1%) is lost to the ambient. All of the parameters used to estimate the thermal losses are given in Table C.1 in Appendix C.

Table 4.1: Summary of thermal losses for 6 cm diameter aperture and all seven lamps on

Variable	Unit	Value
q_{in}	W	9,200
$q_{conv,f}$	W	9,107
q_{ref}	W	92
q_{rerad}	W	1
$q_{conv,i}$	W	0

4.3 Estimating Heat Transfer Through the Aperture Cover

A similar heat transfer analysis is completed to estimate the temperature of the aperture cover surface facing into the cavity and ensure it does not radiate a significant amount of heat into the cavity of the calorimeter. The Monte Carlo simulation results for incident power on the surface of the cover are used in the analysis. As shown in Figure 4.3, the majority of the incident flux is located on the first 3 cm of the cover from the aperture edge for the 6 cm diameter aperture, and the rest of the surface receives negligible radiation. Thus, the analysis assumes all of the power incident on the aperture cover is within the first 3 cm radially outward from the aperture edge where the cooling coils are located for both aperture covers.

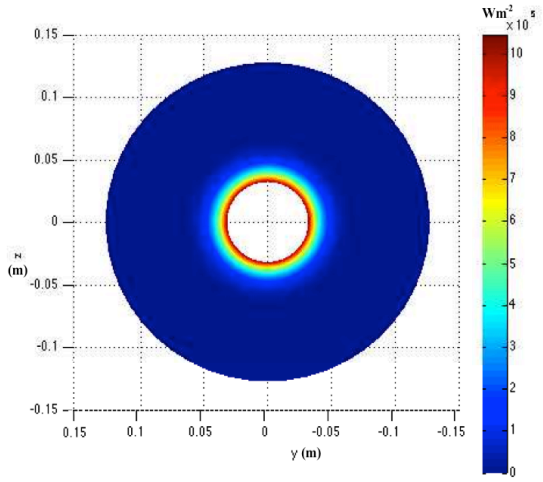

Figure 4.3 Flux distribution map for 6 cm aperture cover and all seven lamps on

An energy balance on the aperture cover at steady state is given by equation (4.24). It is assumed that the major losses are forced convection to the fluid, $q_{conv,f,cov}$, reflection off the cover, $q_{ref,cov}$, and reradiation from the surface to the cavity, $q_{rerad,in}$, and from the surface to outside the calorimeter, $q_{rerad,out}$. Convection is neglected.

$$q_{inc} = q_{conv,f,cov} + q_{ref,cov} + q_{rerad,in} + q_{rerad,out} \tag{4.24}$$

Forced convection to the fluid is described by equation (4.25), where the change in temperature is between the surface of the aperture cover facing away from the cavity and the bulk fluid temperature of the fluid in the coil. The bulk fluid temperature in the coil is calculated using (4.7). The overall heat transfer coefficient-area product is comprised of the resistance due to conduction through the cooling coil tube wall and resistance due to convection of the fluid. The heat transfer coefficient for the fluid is determined using the Nusselt correlation for fully-developed, forced convection flow in a circular curved tube, with uniform wall temperature boundary condition given by equation (4.26), which is verified for $\mathrm{Re_c}(\mathrm{d_{i,c}}/\mathrm{d_{curve}})^{0.5} \geq 80$ and $0.7 \leq \mathrm{Pr_f} \leq 5$ [22]. The diameter of the coil curve, d_{curve}, does not remain constant throughout the cooling coil; therefore, the Nusselt number varies, and the average heat transfer coefficient is found by averaging the heat transfer coefficients associated with the maximum and minimum curve diameters.

$$q_{conv,f,cov} = (UA)_{cov}\,\Delta T \tag{4.25}$$

$$Nu_c = 0.836\left(\mathrm{Re}_c\left(\frac{d_{i,c}}{d_{curve}}\right)^{0.5}\right)^{0.5} \mathrm{Pr}_f{}^{0.1} \tag{4.26}$$

Reflection off the cover is estimated using equation (4.27). The same assumptions as described in section 4.2.2 are used here to approximate the reflectivity of the surface as one minus the surface emissivity. Because the cooling coils cover majority of the aperture area considered, the emissivity of copper is used in the analysis.

$$q_{ref,cov} = (1 - \varepsilon_{Cu}) q_{inc} \tag{4.27}$$

The cavity walls see all of the radiation emitted from the aperture cover surface facing into the cavity, so reradiation losses from the cover to the cavity and from the cover to outside the calorimeter are both defined by equation (4.28), with the temperature, T, being the respective surface temperature.

$$q_{rerad} = A_{cov} \varepsilon_{ss} \sigma T^4 \tag{4.28}$$

The temperature of the surface facing into the cavity can be estimated using equation (4.25), where the change in temperature is between the surface of the cover facing into the cavity and the surface of the cover facing away from the cavity. The overall heat transfer coefficient-area product is comprised of the resistance due to conduction through the tubing, aperture cover walls, and solder and resistance due to convection through the cooling water.

With all of the terms in the energy balance defined, equations (4.3), (4.24), (4.25), (4.27), and (4.28) are solved iteratively in MATLAB. The program converges when the sum of the losses is equal to the energy input into the system, and the cover temperatures in each equation are the same. The wall temperature of the cover surface facing into the cavity is 98.7 °C, and the corresponding reradiation into the cavity is 1.1 W, which is negligible. The parameters used in MATLAB are summarized in Table C.2 in Appendix C.

4.4 Heat Transfer Analysis of High Intensity Flux Regions

4.4.1 *Cavity Walls*

A simple, one-dimensional heat transfer analysis is done to ensure the melting temperature of copper metal is not reached at high intensity flux locations within the cavity. From the Monte Carlo simulations, it is observed that the highest predicted flux from the solar simulator is about 350 kWm^{-2} and occurs on the back wall of the cavity. To determine the steady state temperature of the wall at this location, the one-dimensional model shown in Figure 4.4 is set up.

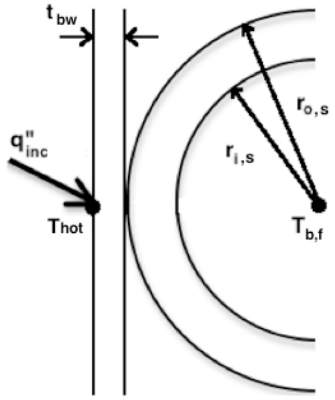

Figure 4.4 Schematic of one-dimensional heat transfer through base wall and spiral tube

The temperature of the wall depends on the incident flux, thicknesses of the base wall, solder, and tube wall, and the temperature of the chilled water. It is also a function of the thermal conductivity of copper and solder, as well as the heat transfer coefficient of the water flowing through the tubing, which is derived in section 4.2.1. Fourier's Law is used to derive a relationship between these parameters, as given in equation (4.29). Because the maximum heat flux occurs at the inlet of the spiral tube, it is assumed that the fluid temperature has not yet increased and is the initial temperature of the chilled water.

$$q''_{inc,bw} = \frac{(T_{hot,s} - T_f)}{\frac{t_{bw}}{k_{Cu}} + \frac{t_{sol}}{k_{sol}} + \frac{r_{o,s}\ln(r_{o,s}/r_{i,s})}{k_{Cu}} + \frac{1}{h_s}} \tag{4.29}$$

The values used to solve for the wall temperature in equation (4.29) are given in Table C.3 of Appendix C, and it is found to be 391°C. The greatest source of resistance in this analysis is the heat transfer coefficient of the flowing water, which is largely dependent on the mass flow rate of the water. For this situation, the water is assumed to be flowing at the designed flow rate of 0.12 kgs^{-1}; it is acknowledged that increasing this number will increase the heat transfer coefficient and help reduce the steady state temperature of the wall. However, because 391°C is well below the melting temperature of copper (1083°C), the mass flow rate is not optimized to minimize this value.

A similar analysis is done on the cavity wall, where the maximum flux is slightly lower, but the fluid temperature is elevated and the only resistance is through the tube wall and flowing water, as shown in Figure 4.5.

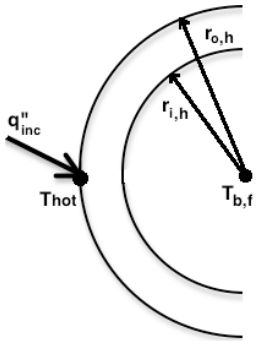

Figure 4.5 Schematic of one-dimensional heat transfer through helical tube

Fourier's Law is used to derive an expression for one-dimensional, steady state heat transfer through the tubing, as shown by equation (4.30). The parameters used for the analysis are given in Table C.4 in Appendix C. The heat transfer coefficient of the water in the helical section of the cavity wall is lower than in the spiral base because of the geometry of the tubing, and because the tubing diameter is larger, at 1.27 cm. This calculation is presented in section 4.2.1. The fluid temperature used in this analysis is the bulk fluid temperature of the water throughout the entire cavity. The steady state wall temperature is found to be 158.6 °C, well below the melting temperature of copper.

$$q''_{inc,h} = \frac{(T_{hot,h} - T_{b,f})}{\frac{r_{o,h}\ln(r_{o,h}/r_{i,h})}{k_{Cu}} + \frac{1}{h_h}} \tag{4.30}$$

4.4.2 *Aperture Cover*

A similar heat transfer analysis is done to ensure the melting temperatures of copper and stainless steel are not reached at the highest intensity flux locations on the aperture cover. From the Monte Carlo simulations, it is observed that the highest predicted flux from the solar simulator onto the aperture cover is 1,000 kWm^{-2} where the cooling coil is not located and 650 kWm^{-2} where the cooling coil is located. To determine the steady state temperature of the cover at these locations, the one-dimensional models shown in Figure 4.6 are evaluated using equations (4.31) and (4.32), which are expressions for heat transfer through the copper tubing and the stainless steel cover, respectively. The parameters used to determine the steady state temperatures are given in Table C.5 in Appendix C. The hottest temperature on the stainless steel cover is calculated to be 520 °C and on the copper cooling coil is 408 °C, both of which are below the respective metal's melting temperature.

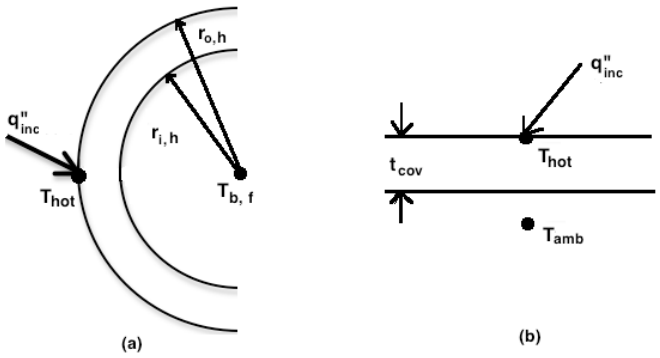

Figure 4.6 Schematic of one-dimensional heat transfer through (a) copper cooling coil and (b) aperture cover.

$$q''_{inc,Cu} = \frac{(T_{hot,cov,Cu} - T_{b,f})}{\frac{r_{o,s}\ln(r_{o,s}/r_{i,s})}{k_{Cu}} + \frac{1}{h_s}} \tag{4.31}$$

$$q''_{inc,ss} = \frac{(T_{hot,cov,ss} - T_{amb})}{\frac{t_{cov}}{k_{ss}} + \frac{1}{h_{air}}} \tag{4.32}$$

4.5 Uncertainty Analysis

The propagation of error method is used to estimate the design stage uncertainty in the measured radiation when using the calorimeter. The sources of error include the flow meter used to measure the mass flow rate of the fluid, the thermopile that measures the temperature difference between the inlet and outlet fluid, and the estimated heat loss from the calorimeter to the ambient. The error due to measuring the flow meter, as stated by the manufacturer, is $u_{\dot{m}} = \pm(0.2\%\ R_{m\_dot})$, where R_{m_dot} is the mass flow rate reading. The uncertainty associated with measuring the fluid temperature difference is a function of the accuracy of the data acquisition unit and the five-junction, type T thermopile and is $u_{\Delta T} = \pm(1\%\ R_T + 0.084\ °C)$, where R_T is the temperature reading [7].

The propagation of error technique uses the linearized approximation of the Taylor series expansion of the given function, which describes how sensitive each variable is to the resultant. The sensitivity is then multiplied by the respective uncertainty, and the resultant's uncertainty is found using the root-sum-square method [7]. For this design, the input energy is related to the measured mass flow rate and temperature difference by equation (4.3). Applying the method described, the uncertainty of the measurement is expressed by equation (4.33).

$$u_{q_{measured}} = \pm\sqrt{\left(\frac{\partial q_{measured}}{\partial \dot{m}} u_{\dot{m}}\right)^2 + \left(\frac{\partial q_{measured}}{\partial \Delta T} u_{\Delta T}\right)^2} \tag{4.33}$$

For a design stage uncertainty analysis, the expected nominal values of each variable are used. To compare the results from this analysis to the results of the current method being used to measure the output of the UMN solar simulator, the same test case from [1] is used: 9.2 kW of power is passed through a 6cm diameter aperture. Table 4.2 summarizes the nominal variable values and constants used to calculate the expected measured energy input and its uncertainty. Using equation (4.33), it is found that $q_{measured}$= 9,107 ± 135 W.

Table 4.2: Summary of nominal values and constants used to calculate $q_{measured}$.

Variable	Nominal Value	Units	Instrument	Precision
$\dot{m}$	0.12	kg s^{-1}	Coriolis mass flow meter	±0.2% reading
ΔT	18.0	°C	5-junction type T thermopile	±1% reading + 0.084 °C
c_p	4187	J kg^{-1} K^{-1}	---	---

The overall uncertainty of the calorimeter is found by summing the measured uncertainty and the estimated heat loss from the calorimeter to the ambient, as shown in equation (4.34). For the considered case, the heat loss is estimated to be 93 W; therefore, the overall uncertainty of the calorimeter is $q_{calorimeter}$ = 9,200 ± 228 W (±2.5%). Whereas the uncertainty of the heat flux gage, as calculated by [1], for the same case is $q_{heat\ flux\ gage}$ = 9,200 ± 1,100 W (±12%).

$$u_{q_{solar}} = u_{q_{measured}} + q_{loss} \tag{4.34}$$

The uncertainty of the calorimeter is also estimated when about 3 kW of power is input into the system through a 6 cm diameter aperture. The measured uncertainty is $q_{measured}$= 2,972 ± 72 W. The estimated heat loss is 28 W, and the overall uncertainty of the calorimeter is estimated to be $q_{calorimeter}$ = 3,000 ± 101 W (±3.4%).

4.6 Conclusion

Using MATLAB to determine the thermal losses with the above analysis, it is found that the sum of the losses accounts for 1% of the total power input for a 6 cm diameter aperture with 9.2 kW and 3 kW of solar power input. Using a one-dimensional heat transfer analysis, it is determined that the locations within the cavity and on the aperture cover where there is high intensity flux will not surpass the melting temperatures of the materials. It is also determined that the radiation from the aperture cover into the cavity is negligible. The uncertainty associated with the heat flux gage measurement currently being used to measure the energy output of the solar

simulator is ±12%, compared to an uncertainty of ±2.5% associated with the calorimeter for the same case.

Chapter 5

Summary

5.1 Summary

An important metric when considering the performance of a solar thermochemical reactor is its efficiency to convert concentrated solar radiation to a chemical fuel. In order to determine a meaningful efficiency, it is important to accurately measure the solar thermal power at the aperture of the reactor. The University of Minnesota uses a high-flux solar simulator to supply the power to a reactor and an optical flux measurement technique to evaluate the power at the focal plane. The current technique has an uncertainty of ±12% associated with it [1]; therefore, a new approach using a fluid cavity calorimeter has been recommended that will more accurately measure the radiative output of the solar simulator. The calorimeter is shown in Figure 5.1 without the surrounding insulation blanket.

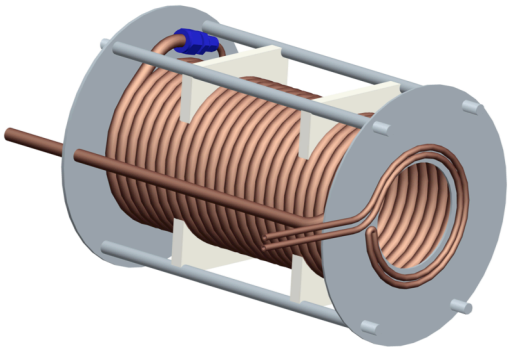

Figure 5.1: Schematic of calorimeter without insulation blanket

The calorimeter is a water-cooled cavity receiver with a detachable front plate, which includes a variable diameter circular aperture. A support structure holds the cavity in place. The cavity is designed using a helically wound copper tube for the walls and a spirally wound copper tube for the base wall. Chilled water enters the inlet of the spiral tube at the center of the base wall, flows through the spiral and helical tubing, and exits at the outlet of the helical tube. The aperture of the calorimeter is placed in the focal plane of the UMN solar simulator. The energy that is incident on the surface of the cavity is conducted through the tubing and convected to the water. The heat gain of the water is directly related to the amount of energy passed into the cavity and can be calculated by measuring the mass flow rate of the water and its temperature difference between the inlet and outlet.

The cavity of the calorimeter is designed using soft, type-L copper tubing. The base wall is made from copper and is added to seal the base of the cavity and increase thermal absorption

within the cavity. The aperture covers are made from stainless steel and have a separate cooling coil soldered around the aperture to reduce heat transfer between the cover and the cavity and to ensure the cover temperature does not surpass the melting temperature of stainless steel. The cooling coils are made from soft, type-L copper tubing. The support structure is comprised of a stainless steel back plate and the aperture cover. The two plates are held in place with four stainless steel spacer rods, each containing a threaded rod to bolt the spacers in place. The cavity is held in place between the plates using four supports made from calcium silicate insulation. The insulation minimizes thermal contact between the cavity and the support structure. The entire cavity is wrapped in Fiberfrax Durablanket insulation to reduce thermal losses from the cavity to the ambient.

To increase the accuracy of the calorimeter measurements, thermal losses from the system are minimized. The geometry of the cavity, material selection, and insulation thickness are all selected to minimize reradation and convective losses. A Monte Carlo ray tracing method is used to predict the incident flux distribution and corresponding power on the surfaces of the cavity. These values are then used to estimate the thermal losses of the system, and it is found that they account for less that 1% of the total power passed through the aperture for both 6 and 10 cm diameter apertures. Accounting for this small percentage of thermal loss and the uncertainty associated with fluid temperature and mass flow rate measurement techniques, the overall uncertainty of the calorimeter is found to be ±2.5% of the power incident at the aperture.

The water-cooled cavity calorimeter design described here has a lower uncertainty associated with measuring concentrated solar flux than the flat-plate calorimeter (±13%) [8], conical cavity calorimeter (±4%) [3], and spherical cavity calorimeter (±5%) [4] described in Chapter 1. The cylindrical cavity calorimeter described by Willoughby [5] has an uncertainty of ±2%; however, the design requires two identical cavities, and the small decrease in possible measured uncertainty does not justify the expense. The conical cavity calorimeter developed at DLR Cologne [6] has an uncertainty of ±0.5% the measured power; however, the difficulty of building a conical cavity with cooling channels in the cavity walls outweighed the small decrease in uncertainty.

5.2 Major Design Assumptions

The following major assumptions were made during the calorimeter design process. When determining the apparent emissivity of the cavity, it is assumed that the cavity surfaces are gray and diffuse. The same assumption is used within the Monte Carlo ray-tracing program,

VeGas. In the program, it is also assumed that the surroundings are non-participating, and emission from the surfaces is neglected.

For the thermal loss analysis, it is assumed that the calorimeter has reached steady state and that the base wall and cylindrical wall of the cavity are isothermal. It is also assumed that the major losses to the ambient are natural convection and reradiation through the aperture; convective losses across the outside of the calorimeter are neglected. An area-averaged cavity wall temperature is used to calculate the natural convection and reradiation losses. The inlet temperature of the fluid is maintained at 5°C, and ambient air temperature is 20°C.

When calculating the heat transfer coefficients of fluid flowing through spiral and helical tubing, Nusselt correlations for the appropriate geometry are used. Both correlations assume the flow is turbulent and fully developed and use a uniform heat flux boundary condition. The property values of the fluid are assumed constant and evaluated at the inlet temperature. The Nusselt correlation to calculate the heat transfer coefficient of air inside the cavity assumes uniformly heated cavity walls. The property values of air are evaluated at ambient temperature.

Bibliography

[1] Krueger, K.R. (2012). *Design and characterization of a concentrating solar simulator*. (Doctoral dissertation).

[2] Krueger, K.R., Davidson, J.H., and Lipiński, W., 2011, "Design of a new 45 kW_e high-flux solar simulator for high-temperature solar thermal and thermochemical research," Journal of Solar Energy Engineering, **133**(1).

[3] Pérez-Rábago, C.A., Marcos, M.J., Romero, and M., Estrada, C.A., 2006, "Heat transfer in a conical cavity calorimeter for measuring thermal power of a point focus concentrator," Solar Energy, **80**(11), pp. 1434-1442.

[4] Glaser, P.E., 1957, "High radiation flux, absolute, water flow calorimeter," Review of Scientific Instruments, **28**(12), pp. 1084-1086.

[5] Willoughby, A.B., 1954, "Absolute water flow calorimeter for the measurement of intense beams of radiant energy," Review of Scientific Instruments, **25**(7), pp. 667-670.

[6] Groer, U. and Neumann, A., 1999, "Development and test of a high flux calorimeter at DLR Cologne," Journal of Physics IV France, **9**(3), pp. 643-648.

[7] Figliola, R.S. and Beasley, D.E. (2000). *Theory and Design for Mechanical Measurements*. New York, NY: John Wiley & Sons.

[8] Jaramillo, O.A., Pérez-Rábago, C.A., Arancibi-Bulnes, C.A., and Estrada, C.A., 2008, "A flat-plate calorimeter for concentrated solar flux evaluation," Renewable Energy **33**(10), pp. 2322-2328.

[9] Siegel, R. and Howell, J. R. (2002). *Thermal Radiation Heat Transfer*. New York, NY: Taylor & Francis.

[10] Sparrow, E. M. and Cess, R. D. (1978). *Radiation Heat Transfer*. New York, NY: McGraw-Hill.

[11] MatWeb Material Properties. Retrieved from: http://www.matweb.com

[12] Emissivity of Common Materials. Retrieved from: http://www.omega.com/literature /transactions/volume1/emissivitya.html

[13] Emissivity Values for Common Materials. Retrieved from: http://www.infrared-thermography.com/material.htm

[14] Do, C. T., Bentz, D. P., and Stutzman, P. E., 2007, "Microstructure and thermal conductivity of hydrated calcium silicate board materials," Journal of Building Physics, **31**(1), pp. 55-67.

[15] Fiberfrax Durablanket S. Retrieved from: http://www.unifrax.com/web/unifraxwebeu.nsf/By+Trade+Name/AD73C921413BBA5F802576C0004F700F/$File/Fiberfrax%20Durablanket%20S%20EN.pdf

[16] Singh, R.P. and Mishra, P., 1980, "Friction factor for Newtonian and non-Newtonian fluid flow in curved pipes." Journal of Chemical Engineering of Japan, **13**(4), pp. 275-280.

[17] Binder, R.C. (1973). *Fluid Mechanics*. Englewood Cliffs, NJ: Prentice-Hall, Inc.

[18] Castiglia, F., Chiovaro, P., Ciofalo, M., Di Liberto, M., Di Maio, P.A., Di Piazza, I., Giardina, M., Mascari, F., Morana, G., and Vella, G., 2010, "Modeling flow and heat transfer in helically colied pipes. Park 3: Assessment of turbulence models, parametrical study and proposed correlations for fully turbulent flow in the case of zero pitch," Report Ricerca di Sistema Elettrico.

[19] Naphon, P. and Wongwises, S., 2002, "Experimental study on the in-tube convection heat transfer coefficients in a spiral coil heat exchanger," Int. Comm. Heat Mass Transfer, **29**(6), pp. 797-809.

[20] Xin, R.C. and Ebadian, M.A., 1997, "The effects of Prandtl numbers on local and average convective heat transfer characteristics in helical pipes," Journal of Heat Transfer, **119**(3), pp. 467-473.

[21] Paitoonsurikarn, S., Lovegrove, K., Hughes, G., and Pye, J., 2011, "Numerical investigation of natural convection loss from cavity receivers in solar dish applications," Journal of Solar Energy Engineering, **133**(2), pp. 021004:1-10.

[22] Kalb, C.E. and Seader, J.D., 1974, "Fully developed viscous flow heat transfer in curved circular tubes with uniform wall temperature," AlChE Journal, **20**(2), pp. 340-346.

[23] Petrasch, J., 2010, "A free and open source Monte Carlo ray tracing program for concentrating solar energy research," Proceedings of the ASME 2010 4th Annual International Conference on Energy Sustainability, Phoenix, AZ, pp.125-132.

[24] Petrasch, J., "VeGaS for optimizing reflector geometries," Zurich Federal Institute of Technology, Zurich, Germany.

[25] Modest, M.F., 2003, "The Monte Carlo method for thermal radiation," Radiative Heat Transfer, Elsevier Science (USA), San Diego, California, pp. 644-679.

[26] "The copper tube handbook," 2010, Copper Development Association Inc., New York, NY.

Appendix A

Pro/Engineer models of the calorimeter components are given below. Figure A.1 shows the cylindrical cavity wall made from helically coiled tubing, and Figure A.2 shows the spiral cooling coil for the base of the cavity. Models of the 6 and 10 cm diameter aperture cooling coils are presented in Figures A.3 and A.4, respectively. The calorimeter support structure requires four spacer rods and four threaded rods; one of each is shown in Figures A.5 and A.6, respectively. Table A.1 gives the required dimensions for each part described above.

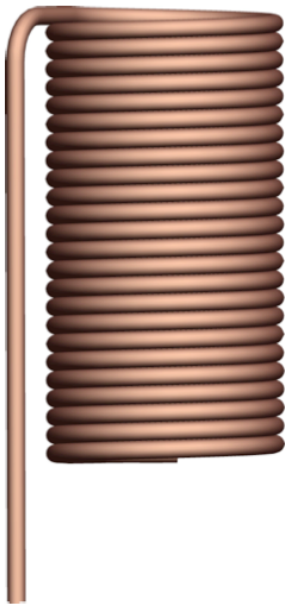

Figure A.1 Helical cooling coil

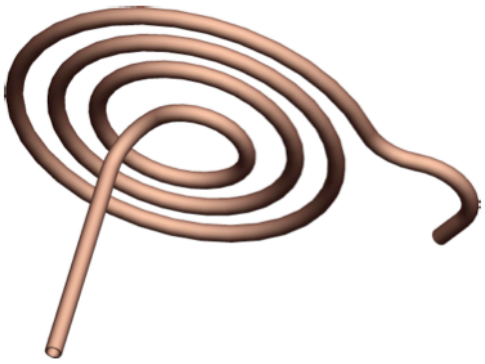

Figure A.2 Spiral cooling coil

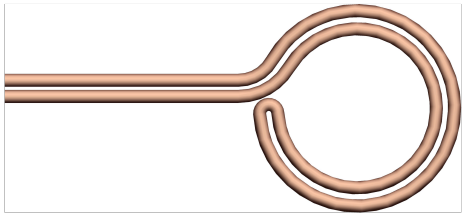

Figure A.3 Cooling coil for 6 cm aperture cover

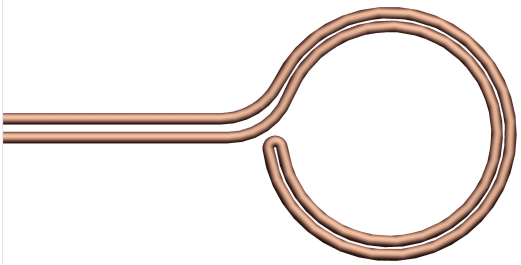

Figure A.4 Cooling coil for 10 cm aperture cover

Figure A.5 Support structure spacer rod

Figure A.6 Support structure threaded rod

Table A.1: Summary of dimensions for the given calorimeter parts (1)

Part	$d_{i,tube}$ (cm)	$d_{o,tube}$ (cm)	L_{tube} (cm)	N	P (cm)	$d_{centerline,helix}$ (cm)	$d_{min,coil}$ (cm)	$d_{max,coil}$ (cm)
Helical Cooling Coil	1.092	1.27	170.96	24	1.27	16.51	--	--
Spiral Cooling Coil	0.386	0.64	110.74	--	--	--	3.81	15.00
6 cm Aperture Cooling Coil	0.386	0.64	78.40	--	--	--	7.39	10.16
10 cm Aperture Cooling Coil	0.386	0.64	107.10	--	--	--	11.39	14.10
Spacer Rod	1.12	1.27	33.02	--	--	--	--	--
Threaded Rod	1.11	--	38.10	--	--	--	--	--

The base wall of the cavity is shown in Figure A.7; it is inserted into the back end of the cylindrical wall, and the spiral cooling coil showed above is soldered to the bottom side of it. Figure A.8 illustrates the back wall of the support structure of the calorimeter and containes holes for the four support rods, as well as the inlet and outlet tubes. The 6 and 10 cm diameter aperture covers are shown in Figures A.9 and A.10, respectively. They also contain four holes to insert the support rods. Table A.2 gives all of their dimensions.

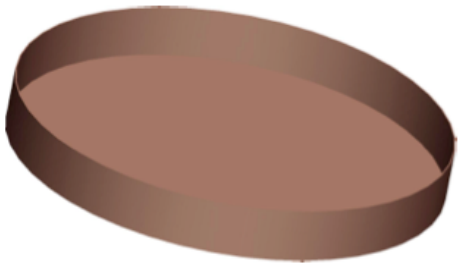

Figure A.7 Cavity base wall

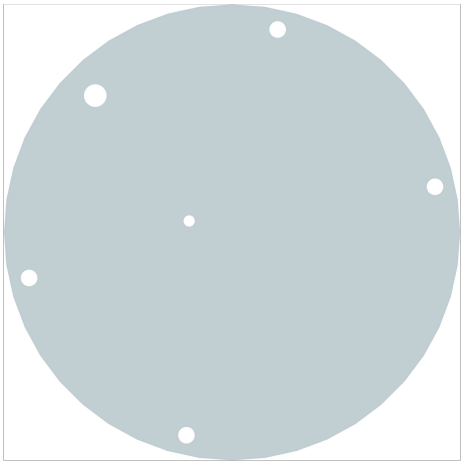

Figure A.8 Calorimeter back wall

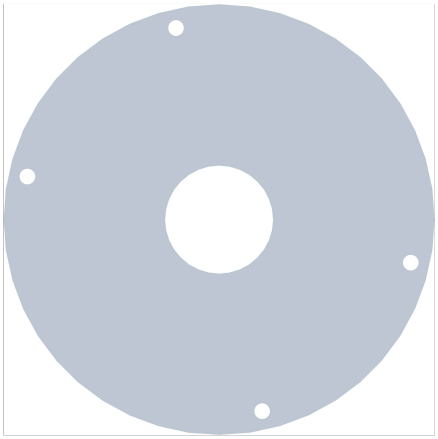

Figure A.9 6 cm diameter aperture cover

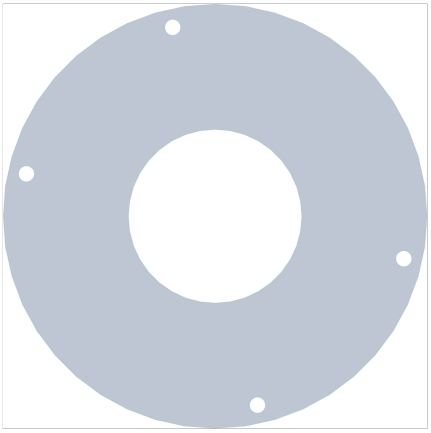

Figure A.10 10 cm diameter aperture cover

Table A.2: Summary of dimensions for the given calorimeter parts (2)

Part	d_o (cm)	d_i (cm)	t (cm)	height (cm)	$d_{bolt\ hole}$ (cm)	$d_{outlet\ hole}$ (cm)	$d_{inlet\ hole}$ (cm)
Base wall	15.24	15.040	0.10	1.65	--	--	--
Calorimeter Back wall	25.40	--	0.32	--	1.11	1.27	0.64
6 cm Diameter Aperture Cover	25.40	6.386	0.238	--	1.11	--	--
10 cm Diameter Aperture Cover	25.40	10.386	0.238	--	1.11	--	--

Appendix B

Results of the Monte Carlo simulation for all seven lamps on and a 10 cm diameter aperture are presented below. The incident flux distribution from the simulator on each surface of the calorimeter is modeled. Note that the length scale and flux scale for each flux map are different. Figure B.1 illustrates the flux distribution on the cylindrical cavity walls and shows the "hot spots" from six of the lamps. Figure B.2 shows the flux distribution on the cavity back wall and the "hot spot" due to the center lamp, and Figure B.3 illustrates the flux distribution on a 10 cm aperture diameter cover.

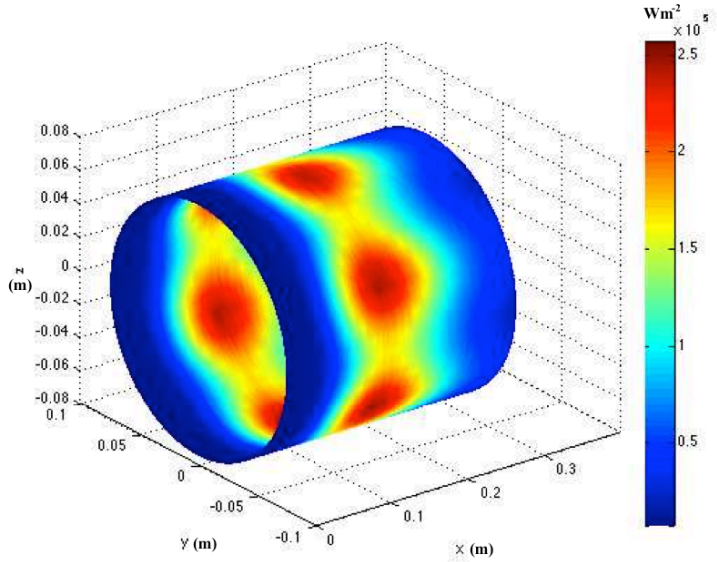

Figure B.1 Flux distribution on cavity wall with 10 cm diameter aperture

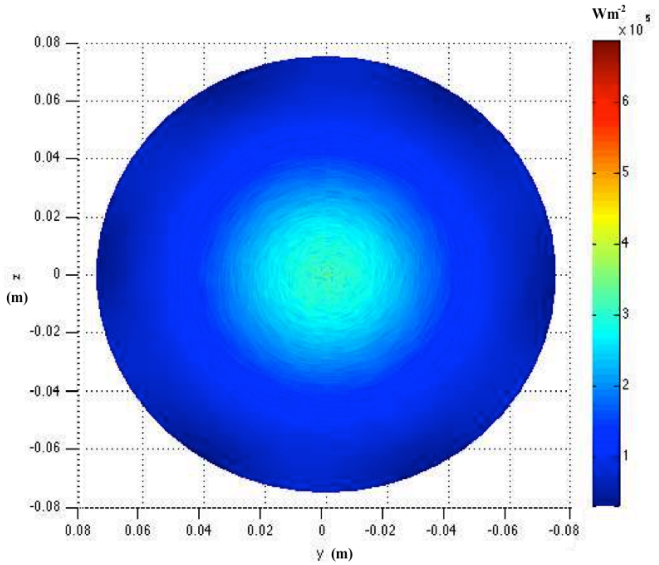

Figure B.2 Flux distribution on cavity back wall with 10 cm diameter aperture

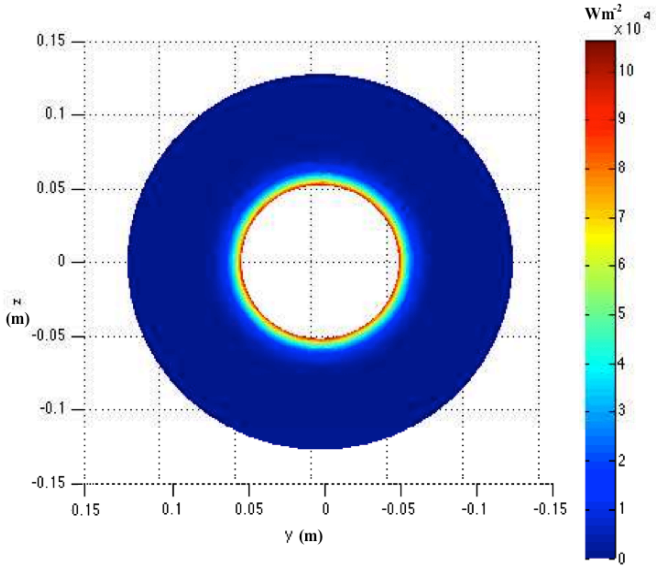

Figure B.3 Flux distribution of aperture cover surface facing simulator with 10 cm diameter aperture

The flux distributions on the surface of the aperture cover facing into the cavity and on the edge of the 10 cm diameter aperture are shown in Figures B.4 and B.5. As with the 6 cm diameter aperture cover, the inner surface of the aperture cover has a low flux distribution due to the relatively low reflectivity of the cavity material and the geometry of the cavity. The incident power over each surface is calculated by integrating the flux over the corresponding surface area. Table 3.5 summarizes the results of the analysis. Table B.1 summarizes the coordinates of the calorimeter surfaces based off the global origin for a 10 cm diameter aperture.

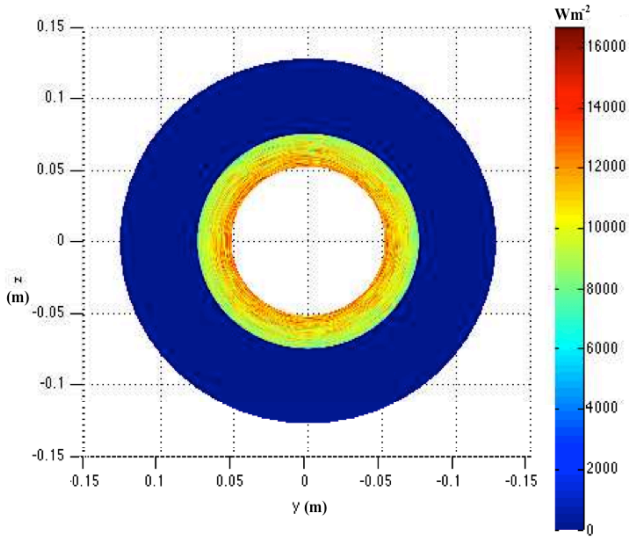

Figure B.4 Flux distribution of aperture cover surface facing into cavity with 10 cm diameter aperture

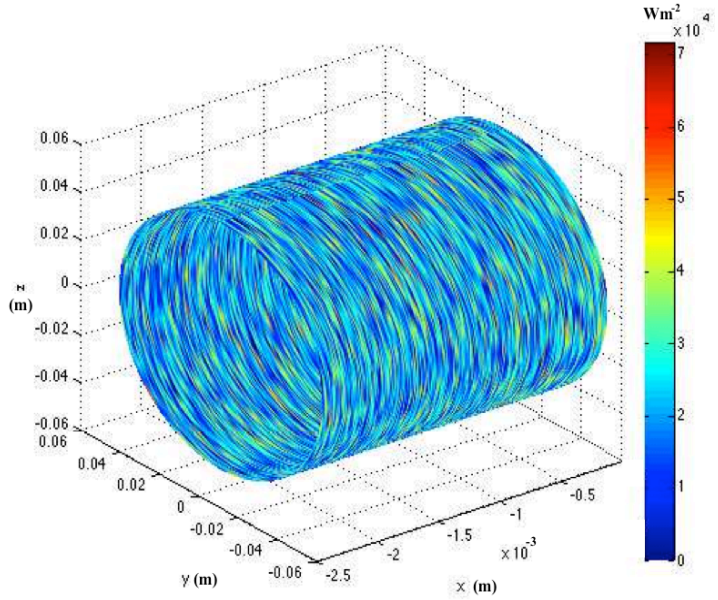

Figure B.5 Flux distribution on aperture edge of 10 cm diameter aperture.

Table B.1: Coordinates of the center and foot points of the cavity and aperture surfaces in the global system centered at the simulator focal point for 10 cm diameter aperture

	Center/foot-point coordinates (m)			Radii (m)		Length (m)
Surface	x	y	z	R_1	R_2	l
Ring 1	0.00000	0.00000	0.00000	0.05184	0.12600	--
Ring 2	0.01900	0.00000	0.00000	0.05184	0.12600	--
Ring 3	-0.30000	0.00000	0.00000	0.00000	0.07000	--
Cylinder 1	-0.30000	0.00000	0.00000	0.07000	0.07000	0.30000
Cylinder 2	0.00000	0.00000	0.00000	0.05184	0.05184	0.00238

Appendix C

The parameters used in MATLAB to solve the heat transfer analyses in Chapter 4 are given in the tables below. All fluid properties are assumed constant and are evaluated at the inlet temperature, because the increase in fluid temperature is not significant.

Table C.1: Parameters to estimate thermal losses

Variable	Unit	Value
A_{sol}	cm^2	27
A_s	cm^2	109
A_{bp}	cm^2	177
$d_{avg,s}$	cm	9.40
$d_{cl,h}$	cm	16.27
h_h	$Wm^{-2}K^{-1}$	6,165
h_s	$Wm^{-2}K^{-1}$	12,780
k_{Cu}	$Wm^{-1}K^{-1}$	398
k_{sol}	$Wm^{-1}K^{-1}$	50
k_f	$Wm^{-1}K^{-1}$	0.58
L_s	m	0.914
Pr_f	--	5
q_{in}	W	12,379
$r_{o,h}$	mm	6.35
$r_{o,s}$	mm	3.20
Re_h	--	17,468
Re_s	--	50,197
$r_{i,h}$	mm	5.46
$r_{i,s}$	mm	1.90
t_{bw}	mm	1.0
t_{sol}	mm	0.5
$T_{f,s,inlet}$	°C	5.0
$T_{f,s,outlet}$	°C	8.5
$T_{h,outlet}$	°C	29.6

Table C.2: Parameters to estimate aperture cover thermal losses

Variable	Unit	Value
A_{cov}	cm^2	64
A_c	cm^2	377
A_{sol}	cm^2	33
$d_{curve,max}$	cm	9.5
$d_{curve,min}$	cm	1.9
$h_{avg,c}$	$Wm^{-2}K^{-1}$	4,209
k_{Cu}	$Wm^{-1}K^{-1}$	398
k_{sol}	$Wm^{-1}K^{-1}$	50
k_{ss}	$Wm^{-1}K^{-1}$	18
L_c	m	1.1
Pr_f	--	5
q_{inc}	W	2309
Re_c	--	17,468
$r_{i,c}$	mm	5.46
$r_{o,c}$	mm	6.35
t_{cov}	mm	9.0
t_{sol}	mm	0.5
$T_{f,c}$	°C	7.3
ε_{Cu}	--	0.78

Table C.3: Parameters for heat transfer model of cavity base wall

Parameter	Unit	Value
h_s	$Wm^{-2}K^{-1}$	9,310
k_{Cu}	$Wm^{-1}K^{-1}$	398
k_{sol}	$Wm^{-1}K^{-1}$	50
$q''_{inc,\ bw}$	Wm^{-2}	350,000
$r_{i,s}$	mm	1.9
$r_{o,s}$	mm	3.2
t_{bw}	mm	1.0
t_{sol}	mm	0.5
T_f	°C	5

Table C.4: Parameters for heat transfer model of cavity wall

Parameter	Unit	Value
h_h	$Wm^{-2}K^{-1}$	6,007
k_{Cu}	$Wm^{-1}K^{-1}$	398
$q''_{inc\ h}$	kWm^{-2}	270
$r_{o,h}$	mm	6.4
$r_{i,h}$	mm	5.5
$T_{b,f}$	°C	20.5

Table C.5: Parameters for heat transfer model for aperture cover

Parameter	Unit	Value
h_{air}	$Wm^{-2}K^{-1}$	9
h_s	$Wm^{-2}K^{-1}$	9,310
k_{Cu}	$Wm^{-1}K^{-1}$	398
k_{ss}	$Wm^{-1}K^{-1}$	18
$q''_{inc, Cu}$	kWm^{-2}	650
$q''_{inc\ ss}$	kWm^{-2}	1,000
$r_{i,s}$	mm	1.9
$r_{o,s}$	mm	3.2
t_{cov}	mm	9.0
T_{amb}	°C	20
$T_{b,f}$	°C	20.5

Appendix D

MatLab code to solve energy balance and compute uncertainty analysis.

```
%Constants
t_bp = 0.001;                                          %base plate thickness [m]
t_solder = 0.0005;                                        %solder thickness [m]
w_solder = 0.003;                                             %solder width [m]
L_s = 0.914;                                            %spiral coil length [m]
A_solder = L_s*w_solder;                                              %solder area
r_cav = 0.075;                                             %cavity radius [m]
L_cav = 0.30;                                              %cavity length [m]
A_cav = 2*pi*r_cav*L_cav;                                   %cavity surface area
r_i_st = 0.0019;                                    %inner radius spiral tube [m]
r_o_st = 0.0032;                                      %out radius spiral tube [m]
d_i_st = 2*r_i_st;                                    %inner diameter spiral tube
r_i_ht = 0.00546;                                   %inner radius helical tube [m]
r_o_ht = 0.00635;                                   %outer radius helical tube [m]
d_i_ht = 2*r_i_ht;                                    %inner diameter helical tube
d_h = 2*r_cav+2*r_o_ht;                               %cavity centerline diameter
N = 24;                                                  %number of helical turns
P = 2*r_o_ht;                                                      %pitch of helix
L_h = sqrt((pi*d_h*N)^2+(N*P)^2);                          %length of helical tube
k_solder = 50;                                  %solder thermal conductivity [W/mK]
k_Cu = 398;                                     %copper thermal conductivity [W/mK]
k_w = 0.58;                                      %water thermal conductivity [W/mK]
nu_w = 1.4E-6;                 %water kinematic viscosity at inlet temp [m^2/s]
rho_w = 1000;                             %water density at inlet temp [kg/m^3]
Pr_w = 5;                                                    %water Prandtl number
D_min_s = 0.0381;                                  %minimum spiral diameter [m]
D_max_s = 0.15;                                    %maximum spiral diameter [m]
D_avg = (D_min_s+D_max_s)/2;                           %average spiral diameter
A_surf_bw =pi*r_cav^2;                                  %base wall surface area
d_ap = 0.06;                                             %aperture diameter [m]
A_ap = pi*d_ap^2/4;                                                %aperture area
emiss_a = 0.99;                                    %cavity apparent emissivity
sigma = 5.67E-8;                                %Stefan Boltzmann constant [W/m^2K^4]
T_amb = 293;                                           %ambient air temperature [K]
k_air = 0.026;                                  %air thermal conductivity [W/mK]
A_surf_c = 2*pi*r_cav*L_cav + pi*r_cav^2;                  %surface area cavity
D_cav = 2*r_cav;                                              %cavity diameter
Pr_air = 0.712;                                %air Prandtl number at ambient temp
g = 9.81;                                                          %gravity [m/s^2]
beta_air = 3.3E-3;              %air thermal expan coeff at ambient temp [1/K]
nu_air = 16E-6;                %air kinematic viscosity at ambient temp [m^2/s]
alpha_air = 2.3E-5;            %air thermal diffusivity at ambient temp [m^2/s]

%%Input fluid mass flow rate and solar power input
m_dot=0.12;                                          %water mass flow rate [kg/s]
q_solar = 9200;                                            %total solar input [W]
q_inc_bw = 0.14*q_solar;              %14 percent q_solar incident on base wall
q_inc_cw = 0.86*q_solar;       %86 percent q_solar incident on clyindrical wall

%%Calculate heat transfer coefficients in spiral and helical tubes
A_st = (pi*d_i_st^2)/4;                          %spiral tube cross section area
v_st = m_dot/(rho_w*A_st);                        %water velocity in spiral tube
Re_s = v_st*d_i_st/nu_w;                       %Reynolds number of fluid in spiral
De_s = Re_s*(d_i_st/D_avg)^0.5;                    %Dean number of fluid in spiral
Nu_s = 27.358*De_s^0.287*Pr_w^-0.949;           %Nusselt number of fluid in spiral
A_ht= (pi*d_i_ht^2)/4;                            %helical tube cross section area
v_ht = m_dot/(rho_w*A_ht);                        %water velocity in helical tube
Re_h = v_ht*d_i_ht/nu_w;                       %Reynolds number of fluid in helix
```

```
Nu_h = 0.00619*Re_h^0.92*Pr_w^0.4*(1+3.455*(d_i_ht/d_h));
                                          %Nusselt number of fluid in helix

h_s_f = Nu_s*k_w/d_i_st;              %heat transfer coefficient in spiral tube
h_h_f = Nu_h*k_w/d_i_ht;                    %heat transfer coefficient in helix

%%Calculate Spiral and Helix UA's
UA_bw = 1/((t_bp/(pi*r_cav^2*k_Cu))+(t_solder/(L_s*w_solder*k_solder))+
        (log(r_o_st/r_i_st)/(2*pi*L_s*k_Cu))+1/(2*pi*L_s*r_i_st*h_s_f));
                  %overall heat transfer coefficient-area product of base wall
UA_cw = 1/(log(r_o_ht/r_i_ht)/(2*pi*L_h*k_Cu)+1/(2*pi*L_h*r_i_ht*h_h_f));
             %overall heat transfer coefficient-area product of cylindrical wall

%%First iteration

%Assume all energy measured by fluid
T_inlet = 278;                                  %inlet fluid temperature [K]
c_p_w = 4204;                          %water specific heat at inlet temp [J/kgK]
q_measured_cw = q_inc_cw;              %assume all input energy measured by fluid
q_measured_bw = q_inc_bw;              %assume all input energy measured by fluid

%Measure Heat Increase in Fluid
T_out_s_initial = q_measured_bw/(m_dot*c_p_w)+T_inlet;
                      %outlet temp from spiral tube/inlet temp of helical tube
T_out_h_initial = q_measured_cw/(m_dot*c_p_w)+T_out_s_initial;
                      %outlet temperature from helical tube
T_bs = (T_inlet + T_out_s_initial)/2;           %bulk fluid temp in spiral tube
T_bh = (T_out_s_initial + T_out_h_initial)/2;  %bulk fluid temp in helical tube

%Convection to Fluid Loss
T_cw = q_measured_cw/UA_cw+T_bh;                  %cylindrical wall temperature
T_bw = q_measured_bw/UA_bw+T_bs;                         %base wall temperature

%From there, "guess" an initial T_wall_avg
T_wall_avg = (T_cw*A_cav+T_bw*A_surf_bw)/(A_cav+A_surf_bw);
             %area-averaged wall temp of cavity to use for rerad and conv losses

%Reradiation Loss
q_reradiation = A_ap*emiss_a*sigma*T_wall_avg^4;    %rerad loss out of aperture

%Natural Convective Loss
L = (4.08*(cos(-0.11))^5.41*D_cav)+(-1.17*(cos(-0.30))^7.17*L_cav)+(0.07*(cos(
     0.08))^1.99*d_ap);                                %characteristic cavity length
Ra_inside = g*beta_air*abs((T_wall_avg-T_amb))*L^3/(nu_air*alpha_air);
                                                 %Rayleigh number air inside cavity
Nu_inside=0.0196*Ra_inside^0.41*Pr_air^0.13;  %Nusselt number air inside cavity
h_inside = Nu_inside*k_air/L;   %heat transfer coeff air inside cavity [W/m^2K]
q_conv_inside = h_inside*A_surf_c*(T_wall_avg-T_amb);
                                       %natural convection loss out of aperture

%Reflection Loss
q_reflected = (1-emiss_a)*q_solar;             %reflection loss out of aperture

%%Iterate to solve energy balance

i=1; %counter
q_loss(i) = q_reflected + q_conv_inside + q_reradiation;
       %loss term defined as sum of rerad, natural conv, and reflection out of
        aperture (forced conv to fluid considered separately)

T_difference = 100;        %variable (arbitrarily set) to determine convergence
```

```
%difference between area-averaged wall temperatures (i) and (i-1)(T_difference)
must be less than 0.000001 to converge

while T_difference > 0.000001
q_new_measured_total(i) = q_solar - q_loss(i);                  %energy balance

q_area_avg_cw_new_measured(i) =q_new_measured_total(i).*(A_cav/(A_cav+A_surf_bw
));                        %area-average new measured input onto cylindrical wall
q_area_avg_bw_new_measured(i) = q_new_measured_total(i).*(A_surf_bw/(A_cav+
A_surf_bw));                       %area-average new measured input onto base wall

T_out_s_new(i) = q_area_avg_bw_new_measured(i)./(m_dot*c_p_w)+T_inlet;
                          %new spiral outlet fluid temp/helical inlet fluid temp
T_out_h_new(i) = q_area_avg_cw_new_measured(i)./(m_dot*c_p_w)+T_out_s_new(i);
                                                  %new helical fluid outlet temp

T_bs(i) = (T_inlet + T_out_s_new(i))/2;             %spiral tube bulk fluid temp
T_bh(i) = (T_out_s_new(i) + T_out_h_new(i))/2;    %helical tube bulk fluid temp

T_cw_new(i) = q_area_avg_cw_new_measured(i)./UA_cw+T_bh(i); %new cyl. wall temp
T_bw_new(i) = q_area_avg_bw_new_measured(i)./UA_bw+T_bs(i); %new base wall temp

T_wall_avg_new(i) = (T_cw_new(i).*A_cav+T_bw_new(i).*A_surf_bw)/(A_cav+
A_surf_bw);                                     %new area-averaged cavity wall temp

q_reradiation_new(i) = A_ap*emiss_a*sigma*T_wall_avg_new(i).^4; %new rerad loss

Ra_inside_new(i) = g*beta_air*abs((T_wall_avg_new(i)-T_amb))*L^3/(nu_air*
alpha_air);                                                %new air Rayleigh number
Nu_inside_new(i)=0.0196*Ra_inside_new(i).^0.41*Pr_air^0.13;  %new air Nu number
h_inside_new(i) = Nu_inside_new(i).*k_air/L; %new air heat transfer coefficient
q_conv_inside_new(i) = h_inside_new(i).*A_surf_c*(T_wall_avg_new(i)-T_amb);
                                                    %new natural convection loss

q_new_losses(i) = q_reflected + q_reradiation_new(i) + q_conv_inside_new(i);
                                                                %new sum of losses

T_difference(i) = abs(T_wall_avg_new(i) - T_wall_avg(i));
                 %check wall temperature difference between iterations i and i-1

%counter adjusting
q_loss(i+1) = q_new_losses(i);
q_reradiation(i+1) = q_reradiation_new(i);
q_conv_inside(i+1) = q_conv_inside_new(i);
T_wall_avg(i+1) = T_wall_avg_new(i);
i=i+1;
end

%%Output
deltaT = T_out_h_new(i-1)-T_inlet        %inlet and outlet change in fluid temp
q_conv_fluid = q_new_measured_total(i-1)   %amount of energy convected to fluid
u_measured = sqrt((c_p_w*(T_out_h_new(i-1)-T_inlet)*m_dot*0.002)^2+(c_p_w*m_dot
*(((T_out_h_new(i-1)-T_inlet)*0.01+0.084)))^2)    %uncertainty in measured heat
losses = q_new_losses(i-1)                           %thermal losses to ambient
u_calorimeter = u_measured+q_new_losses(i-1)%overall uncertainty in calorimeter
percent_uncertainty = u_calorimeter/q_solar*100            %percent uncertainty
```

Table D.1: Matlab heat transfer program flowchart